Computational Mechanics
https://doi.org/10.1007/s00466-026-02826-2

ORIGINAL PAPER

Targeted attenuation of spurious reflections in coupled wave propagation simulations

Kin Fung Chan[1] · Nicola Bombace[2] · Simone Falco[1] · David Chapman[1] · Nik Petrinic[1] · Daniel Eakins[1]

Received: 13 December 2025 / Revised: 29 June 2026 / Accepted: 2 July 2026

Abstract
Unphysical wave reflections pollute a domain's solution when high frequency waves propagate from a fine to a coarse spatial discretisation. Inspired by the selective perfect matching layer, we look to specifically target and dampen the incompatible frequencies that cause the energy entrapment of spurious waves. In this work, we propose a Shepard-based projection method that filters with the inverse-distance weighting kernel—an alternative and simple to implement basis. We demonstrate the method in dynamically coupled finite element subdomains, that vary not only in mesh size, but also respective time steps. The attenuation is applied to a two-subdomain coupling, where explicit computations are leveraged to obtain a coarse-field representation of an interface. Performance of the proposed filter demonstrates a 99% attenuation of spurious reflections across a wide range of incompatible frequencies. Furthermore, through combining the Shepard-based projection with multi-time step integration and non-matching meshes, significant speedups in runtime can be achieved.

Keywords Spurious wave · Filtering · Perfect matching layer · Stress wave propagation · Finite element

1 Introduction

The numerical simulation of highly dynamic engineering structures increasingly relies on the spatial discretisation with techniques such as finite elements or collocation points, arranged in meshes or grids. In practice, these discretisations are seldom uniform in space, with regions of interest requiring fine meshes to capture complex stress wave behaviour or non-linearities, while other areas can be represented by coarser meshes to save computational cost. When different regions or subdomains are modelled together, variation in mesh density or grid spacing becomes inevitable. A well-known source of numerical error, involving non-uniform computational grids, is spurious wave reflection. As found in the seminal work of Bažant, the presence of an unphysical wave reflection is significant at mesh transitions between coarse and fine finite elements [1]. To elaborate, the work uncovered that even for variations in element sizes of 10%, spurious reflections still pollute the solution of a propagating wave from a fine mesh. Gradually increasing element sizes via a transition region mitigates the phenomenon, however this is only effective for very small ratios between large and small element sizes [2, 3]. Numerical impedance mismatch can be found in several continuum settings, some of these include adaptive mesh refinement, damage, or multi-physics couplings [4–8]. However, the artifact is not limited to the continuum, and applications coupling multi-scale regimes like atomistic or molecular dynamics coupled simulations, also suffer from pronounced unphysical reflection [9, 10]. In this work, we focus on the reflected wave within an explicit finite element framework. The coupling of subdomains with varying mesh discretisations leads to incorrect stress distributions and the entrapment of energy within the finest spatial discretisation.

A distinction in phenomena must be made when considering spurious reflections amongst other forms of numerical errors, specifically numerical dispersion and general spurious oscillations. In transient finite element method (FEM) solutions, Jiang and Rogers elucidated how discretisation leads to frequencies beyond a certain cut-off (highest natural frequency) being eliminated [11]. These higher modes are represented with considerable error [12, 13]. Analogous to the Gibbs' or "Gibbs-Wilbraham" phenomenon in Fourier

✉ Kin Fung Chan
kin.chan@eng.ox.ac.uk

[1] Department of Engineering Science, University of Oxford, Parks Road, Oxford OX1 3PJ, England, UK

[2] AMD Inc., Edinburgh Technopole, Bush Loan, Edinburgh EH26 0PY, Scotland, UK

Published online: 29 July 2026

approximations of discontinuities, the numerical solution overshoots the analytical solution in a step, followed by oscillations in decreasing amplitude [14, 15]. Whilst methods, such as low-pass filters, exist for eliminating high frequency oscillations, not all can be used for targeting the broad range of frequencies that originate from the interface of non-uniform meshes or grids [16, 17]. This will be crucial for assessing approaches targeting the attenuation of spurious wave reflection frequencies.

1.1 Previous work on attenuation

Starting from the foundational work of von Neumann and Richtmyer, the Bulk Viscosity method is widely employed, originating in fluid mechanics for simulating hydrodynamic shocks [18]. The damping effect involves an additional contribution to the stress tensor, where its effectiveness depends on material parameters of the subdomain. Despite being a good fit for discontinuous loadings like shocks, its insensitivity to meshing irregularities does not make it a universal remedy to spurious reflections [19, 20]. Filtering in the time-domain is an alternative method to bulk viscosity, where key works by Holmes and Belytschko have described a non-intrusive method that can be applied as a post-processing step to solutions containing numerical dispersion [15]. These estimate the natural frequencies of a mesh, attenuating a kinematic output based on a finite window of consecutive time steps. The main caveat of such methods is its usage as a post-processing tool. Dissipative time integration schemes incorporate similar ideas to reduce non-physical oscillations, key ideas for those that are explicit time integrators can be found in the works of Hulbert and Chung [21]. Recent works in the temporal domain include those such as the Bathe time integration scheme, the pushforward-pullback (PFPB) method and schemes that march in time with dissipative control utilising local computation of integration parameters [22–25]. Whilst these methods are effective, they can lead to undesirable instabilities, complex parameter calibration, as well as low frequency damping [26].

Simulating physical phenomena within an infinite or unbounded domain necessitates the suppression of wave reflections too. For this purpose, methods such as Absorbing Boundary Conditions (ABCs) and the Perfectly Matched Layer (PML) are employed to manage a finite domain by effectively mitigating boundary reflections [27]. Initially proposed by Bérenger, the PML has been extended beyond absorbing electromagnetic waves to mechanical waves [28, 29]. The PML dampens all frequencies of waves, whilst requiring fine-tuning of layer thickness, absorption profiles and often a high computational cost. Consequently, the Selective Perfect Matching Layer (SPML) enables the control of frequencies being filtered to just those incompatible with subdomain meshes, as well as defining projection operators that are more convenient to form than the aforementioned [26]. The method also combines the capability of coupling with spurious wave reflection attenuation. Marchais et al. constructed multiple projection operators for which 99% of the reflected energy can be removed from the system. For this reason, the method will prove as a strong benchmark to match.

Prevention of spurious wave reflection is also referred to in the coupling methods of Xiao and Belytschko's Bridging Domain Method, as well as the Arlequin Method [30, 31]. These concurrent multi-scale coupling approaches share the solution of Lagrange multiplier fields in an overlapping zone. Hence, these methods naturally dissipate and reduce spurious wave reflections without requiring additional damping procedures. The main caveat being a larger overhead, through solving a system of equations, that leads to limited scalability. Despite this clear limitation, they are flexible in allowing for the coupling of subdomains that do not require the same numerical method, as seen in Tu et al. [32]. For this reason, versatility of a proposed spurious wave correction method is key on top of aforementioned characteristics.

In summary, while many techniques exist for managing numerical dispersion across multiple physics regimes, few address the specific issue of reflections from incompatible meshes. Those that do, have not shown to fulfil all of the following criteria:

- Provide numerical dissipation specifically targeting spurious reflective frequencies,
- Attenuate during the time integration of a dynamic simulation, rather than as a post-processing step,
- Avoid the requirement of constructing a mesh (connectivity) for filtering in,
- Combine methods with multi-time step integration and non-matching meshes to improve computational performance.

1.2 A motivating example

To depict the numerical artifact in question, an exemplary elastodynamic 1-D problem is introduced. Considering a long homogeneous bar of length $L = 250$ mm in Fig. 1, partitioned into two consecutive subdomains with two separate mesh sizes. We partition the domain into a small and a large subdomain. The smaller of the two element sizes is of characteristic length $h_s = 0.25$ mm, with the larger elements $h_L = 1.0$ mm, where a total of 500 small and 125 elements gives lengths $L_s = L_L = 125$mm. Elastic material properties, representative of a steel alloy, are constant throughout the bar with Young's modulus $E_s = E_L = 207$ GPa and density $\rho = 7.83 \times 10^{-6}$ kgmm^{-3}. Each simulation is advanced through time with explicit integration over a single time step, where we hereby call a monolithic simulation. The Courant

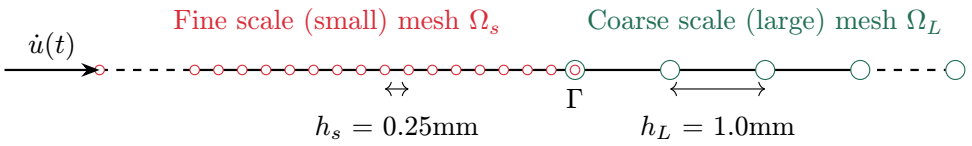

Fig. 1 Demonstration setup of spurious wave reflection in 1-D elastic bar of two varying spatial discretisations coupled at interface Γ with a velocity boundary condition $\dot{u}(t)$ varied in frequency ω

number $Co = 0.5$ is applied to Δt of the entire domain. In later simulations, we will look to extend this by employing multiple time steps. At $x = 0$ mm, a velocity boundary condition $\dot{u}(t)$ is applied as the following:

$$\dot{u}(t) = \begin{cases} 10 \sin(2\pi\omega t), & \text{if } t < L/4c \\ 0, & \text{otherwise} \end{cases} \tag{1}$$

where we vary the frequency $\omega = c/\lambda$ of the incident wave through defining the dilatational wave speed $c = \sqrt{E/\rho}$ and wavelength λ as a function of L_s. This leads to repeating the simulation for $\lambda \in \{L_s/4, L_s/8, \ldots, L_s/68\}$. In Fig. 2, we present 6 of the 17 monochromatic wavelengths simulated as the incident wave is fully applied at $t = 0.01216$ ms, where the wave reaches half the length of L_s. Starting with a low frequency in (a) of Fig. 2, we gradually increase the frequency to (f).

At $t = 0.03647$ ms, the wave interacts with the interface, Γ, of the two spatial discretisations, and the transmitted wave reaches half the length of L_L. Figure 3 depicts the issue of spurious wave reflection, as h_L is too large to capture higher variations of ω. From the low frequency in (a), a smooth propagation of the wave is visible from small to large mesh. As ω is increased in (b) to (c), a deterioration in the solution is visible in the large mesh. A significant spurious reflection is visible in (d), with (e) and (f) showing a near complete reflection of the wave back into the small mesh - an unphysical solution.

The energy associated to the transmission and reflection of the elastic wave is portrayed in Fig. 4, where each incident frequency ω can be represented as its wavelength λ. Each simulation computes the kinetic and internal energies at $t = 0.03647$ ms, where larger wavelengths are smoothly transmitted from fine to coarse, in contrast smaller wavelengths (higher frequencies) are reflected back. This gives rise to the term *energy entrapment*, where higher frequency data is trapped within the finest spatial discretisation. Further details on the reflected energy is well documented in the works of Zafati and Al Hout [33]. We truncate the plotted dataset, ignoring the longer wavelengths than $10\times$ the large element size h_L. For this, we verify Bažant's comment of requiring $10\times$ the highest frequency to be a reasonable approximation of a wave, but also a rather conservative conclusion [1]. The Nyquist-Shannon sampling theorem is also of interest when considering the frequency at which this transition occurs [34]. Defined as the cut-off frequency $\omega_c = 2c/h_L$, we plot the equivalent wavelength at $\lambda = 4$ mm for this example. The highlighted green region highlights the frequency spectrum for which this work looks to target. In this region spurious wave reflection is evident, as well as a deterioration of the wave's solution.

This paper is organised as follows. The following Section 2 outlines the governing equations of the continuum, where the partitioned equations of motion are provided. In Section 3, we elaborate upon those previously mentioned methods of filtering, expanding on their usage in coupled finite element algorithms. The proposed method of spurious wave attenuation is detailed in Section 4. Coupling explicit finite element subdomains with dissipation is described in Section 5. In Section 6, a comparison of the attenuating methods is made, together with numerical examples that aid the evaluation of the proposed approach. Section 7 closes with conclusions and discussions for future work.

2 General formulation

The approach for determining the deformation of a solid body $\Omega \subset \mathbb{R}^d$, for dimension $(\cdot)^d$, is the partitioning into two non-overlapping subdomains Ω_s and Ω_L as follows:

$$\Omega = \Omega_s \cup \Omega_L; \quad \Omega_s \cap \Omega_L = \emptyset; \quad \Gamma \subset \partial\Omega_s \cap \partial\Omega_L \tag{2}$$

where the interface between the two subdomains is denoted Γ, but not the entire boundaries of subdomains $\partial\Omega$. Starting from the local momentum balance of each subdomain, the strong to weak form is achieved through the principle of virtual power.

2.1 A partitioned continuum model

Consider the strong form of the dynamic equilibrium for a coupled problem between two subdomains Ω_s and Ω_L as:

$$\rho_s \ddot{\mathbf{u}}_s - \nabla \cdot \boldsymbol{\sigma}_s - \rho_s \mathbf{b}_s = 0, \text{ in } \Omega_s \times [0, T] \tag{3}$$

$$\rho_L \ddot{\mathbf{u}}_L - \nabla \cdot \boldsymbol{\sigma}_L - \rho_L \mathbf{b}_L = 0, \text{ in } \Omega_L \times [0, T] \tag{4}$$

$$\ddot{\mathbf{u}}_s = \ddot{\mathbf{u}}_L \text{ on } \Gamma \tag{5}$$

$$\mathbf{t}_s = \mathbf{t}_L \text{ on } \Gamma \tag{6}$$

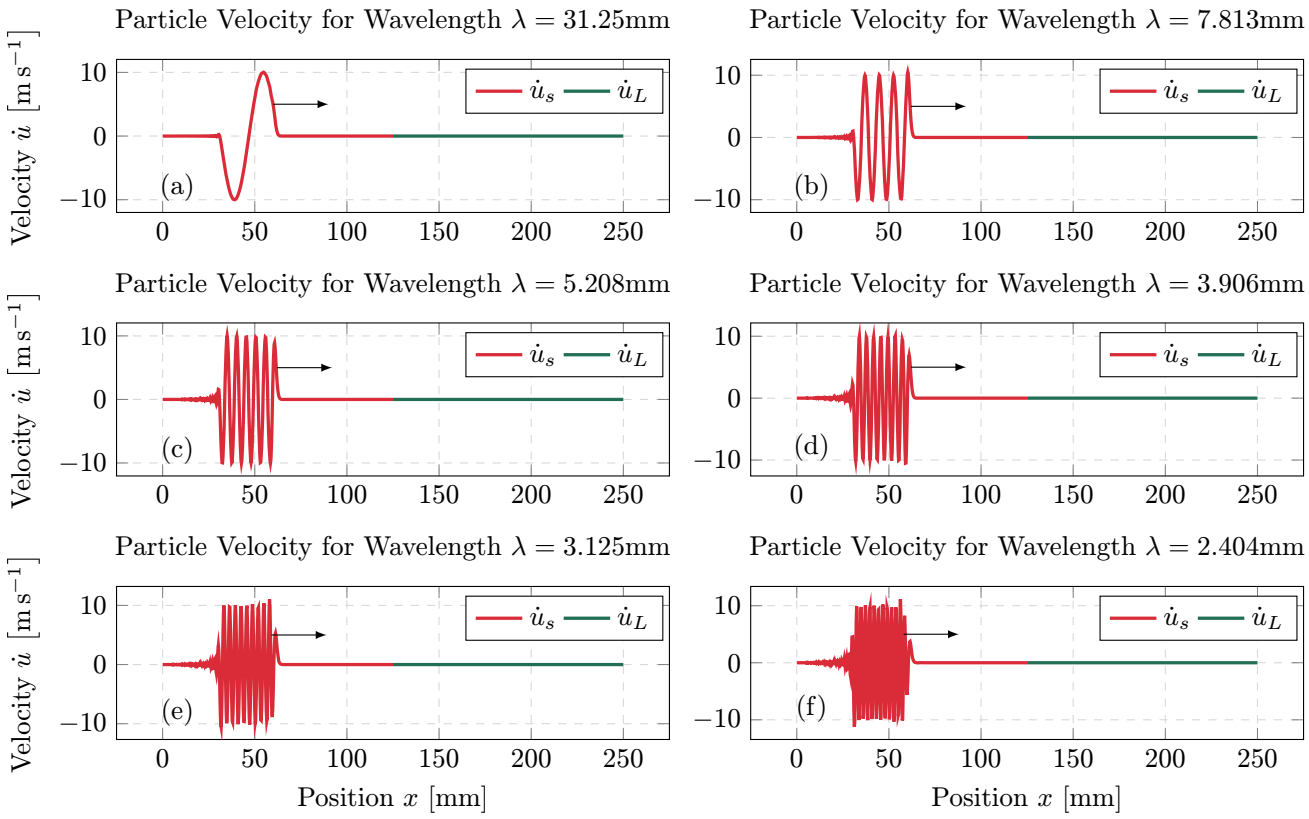

Fig. 2 Velocity distributions of an incident wave at $t = 0.01216$ ms for the monochromatic frequency study demonstrating spurious wave reflection through 1D elastic bar of discretisations $h_s = 0.25$ mm and $h_L = 1.0$ mm, integrating with single time step

where for each subdomain Ω_i, we denote material density ρ_i, acceleration $\ddot{\mathbf{u}}_i$, divergence of the Cauchy stress tensor $\nabla \cdot \boldsymbol{\sigma}_i$, body forces per unit volume $\rho_i \mathbf{b}_i$. Continuity of accelerations $\ddot{\mathbf{u}}_i$ and tractions $\mathbf{t}_i$ on interface Γ is enforced. The weak form of the momentum equation, in an updated Lagrangian formulation, gives the virtual power:

$$\delta P_s(\delta \dot{\mathbf{u}}_s, \dot{\mathbf{u}}_s) = \delta P_s^{\text{kin}} + \delta P_s^{\text{int}} - \delta P_s^{\text{ext}} = 0 \tag{7}$$

$$\delta P_L(\delta \dot{\mathbf{u}}_L, \dot{\mathbf{u}}_L) = \delta P_L^{\text{kin}} + \delta P_L^{\text{int}} - \delta P_L^{\text{ext}} = 0 \tag{8}$$

where we define $P_i^{\text{kin}}, \delta P_i^{\text{int}}, \delta P_i^{\text{ext}}$ as kinetic, internal and external components of power with a finite element space of admissible virtual velocities $\delta \dot{\mathbf{u}}_i(\mathbf{X}_i) \in \mathcal{V}_0$ for each Ω_i, enabling the variational formulation as follows:

$$\begin{aligned} &\int_{\Omega_s} \rho_s \ddot{\mathbf{u}}_s \cdot \delta \dot{\mathbf{u}}_s \mathrm{d}\Omega + \int_{\Omega_s} \boldsymbol{\sigma}_s \cdot \delta \mathbf{D}_s \mathrm{d}\Omega \\ &- \int_{\Omega_s} \rho_s \mathbf{b}_s \cdot \delta \dot{\mathbf{u}}_s \mathrm{d}\Omega - \int_{\Gamma_s} \mathbf{t}_s \cdot \delta \dot{\mathbf{u}}_s \mathrm{d}\Gamma = 0 \\ &\int_{\Omega_L} \rho_L \ddot{\mathbf{u}}_L \cdot \delta \dot{\mathbf{u}}_L \mathrm{d}\Omega + \int_{\Omega_L} \boldsymbol{\sigma}_L \cdot \delta \mathbf{D}_L \mathrm{d}\Omega \\ &- \int_{\Omega_L} \rho_L \mathbf{b}_L \cdot \delta \dot{\mathbf{u}}_L \mathrm{d}\Omega - \int_{\Gamma_L} \mathbf{t}_L \cdot \delta \dot{\mathbf{u}}_L \mathrm{d}\Gamma = 0 \end{aligned} \tag{9, 10}$$

2.2 Explicit finite element discretisation

Discretising both subdomains into finite elements Ω_e, we approximate the test function with Lagrangian shape functions N_i as $\delta \dot{\mathbf{u}}(\mathbf{X}) = \delta \dot{\mathbf{u}}_i N_i(\mathbf{X})$. This enables the velocity field to be approximated by nodal variables:

$$\dot{\mathbf{u}}(\mathbf{X}, t) \approx \sum_{i=1}^{\mathcal{N}_n} \mathbf{N}_i(\mathbf{X}) \dot{\mathbf{u}}_i(t) = \mathbf{N}_i(\mathbf{X}) \dot{\mathbf{u}}_i(t) \tag{11}$$

where the displacements are similarly given by:

$$\mathbf{u}(\mathbf{X}, t) = \mathbf{N}_i(\mathbf{X}) \mathbf{u}_i(t) \tag{12}$$

To incorporate time dependence into the approximation of motion with finite elements, the velocity gradient is computed with the derivatives of the shape functions:

$$\nabla \mathbf{v} = \dot{\mathbf{u}}_i \nabla \mathbf{N}_i(\mathbf{X}) \tag{13}$$

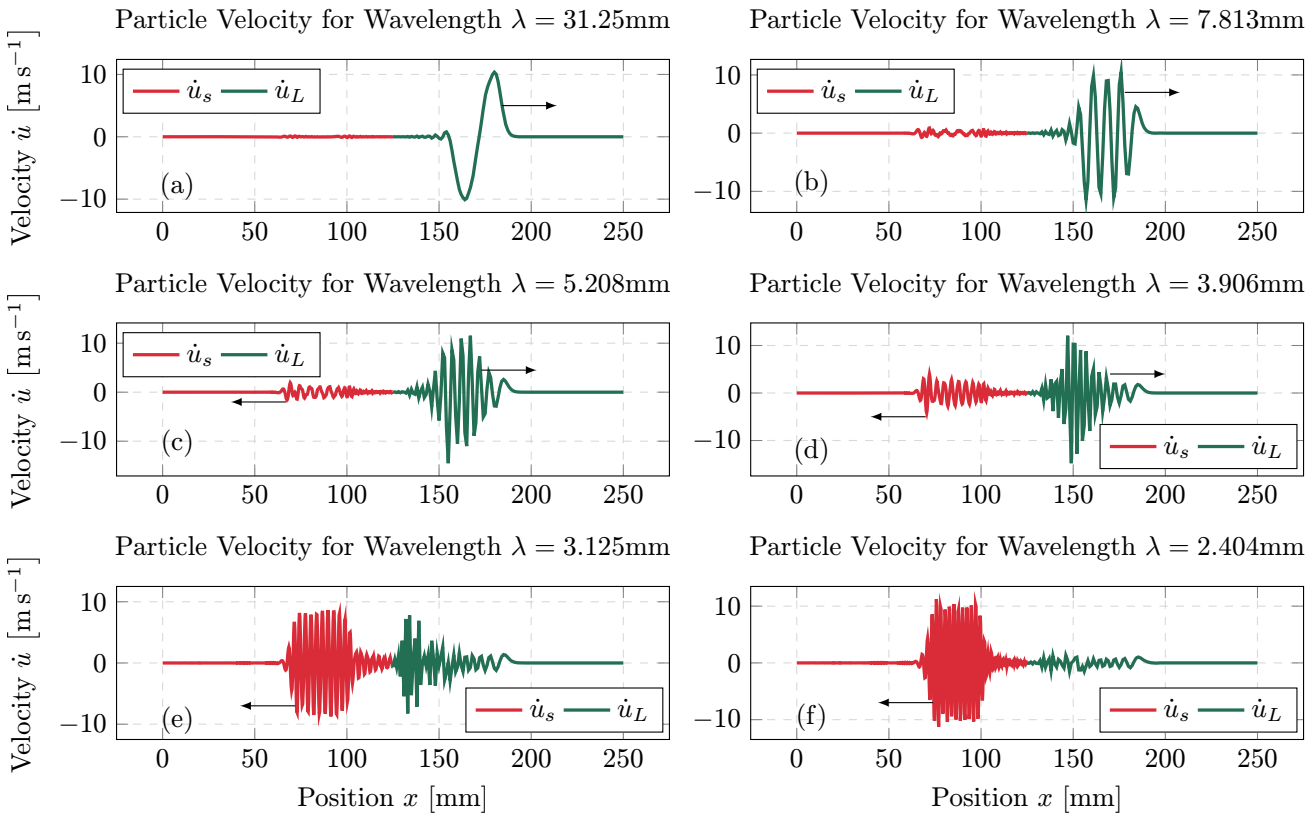

Fig. 3 Velocity distributions after interface Γ interaction at $t = 0.03647$ ms for the monochromatic frequency study demonstrating spurious wave reflection through a 1D elastic bar of discretisations $h_s = 0.25$ mm and $h_L = 1.0$ mm, integrating with single time step

To enable the discretised form of the dynamic equilibrium equation, the approximation of the test function with shape functions is substituted into the virtual power of Eqs. 7 - 8. Assuming negligible body forces, each of these nodal forces can now be computed as:

$$\begin{aligned}
\mathbf{f}_s^{\text{kin}} &= \int_{\Omega_s} \rho_s \mathbf{N}^{\mathrm{T}} \mathbf{N} \ddot{\mathbf{u}}_s \ \mathrm{d}\Omega; \\
\mathbf{f}_s^{\text{int}} &= \int_{\Omega_s} \mathbf{B}_s^{\mathrm{T}} \boldsymbol{\sigma}_s \ \mathrm{d}\Omega; \\
\mathbf{f}_s^{\text{ext}} &= \int_{\Omega_s} \rho_s \mathbf{b}_s \ \mathrm{d}\Omega + \mathbf{N}^{\mathrm{T}} \mathbf{t}_s|_{\Gamma}
\end{aligned} \tag{14}$$

$$\begin{aligned}
\mathbf{f}_L^{\text{kin}} &= \int_{\Omega_L} \rho_L \mathbf{N}^{\mathrm{T}} \mathbf{N} \ddot{\mathbf{u}}_L \ \mathrm{d}\Omega; \\
\mathbf{f}_L^{\text{int}} &= \int_{\Omega_L} \mathbf{B}_L^{\mathrm{T}} \boldsymbol{\sigma}_L \ \mathrm{d}\Omega; \\
\mathbf{f}_L^{\text{ext}} &= \int_{\Omega_L} \rho_L \mathbf{b}_L \ \mathrm{d}\Omega + \mathbf{N}^{\mathrm{T}} \mathbf{t}_L|_{\Gamma}
\end{aligned} \tag{15}$$

where the inertial contribution can also be written through the approximation of a lumped mass matrix with acceleration:

$$\mathbf{M}_e = \sum_{e=1}^{\mathcal{N}_e} \int_{\Omega_e} \rho \mathbf{N}^{\mathrm{T}} \mathbf{N} \ \mathrm{d}\Omega_e \tag{16}$$

At the global level, both subdomains are assembled in vectorised form, with dimensions corresponding to the number of nodes $\mathcal{N}_{n_s}$ and $\mathcal{N}_{n_L}$, to form the following:

$$\mathbf{M}_s = \begin{bmatrix} \mathbf{M}_{s1} \\ \mathbf{M}_{s2} \\ \vdots \\ \mathbf{M}_{d\mathcal{N}_{n_s}} \end{bmatrix}; \quad \mathbf{f}_s^{\text{ext}} = \begin{bmatrix} \mathbf{f}_{s1}^{\text{ext}} \\ \mathbf{f}_{s2}^{\text{ext}} \\ \vdots \\ \mathbf{f}_{d\mathcal{N}_{n_s}}^{\text{ext}} \end{bmatrix}; \quad \mathbf{f}_s^{\text{int}} = \begin{bmatrix} \mathbf{f}_{s1}^{\text{int}} \\ \mathbf{f}_{s2}^{\text{int}} \\ \vdots \\ \mathbf{f}_{d\mathcal{N}_{n_s}}^{\text{int}} \end{bmatrix} \tag{17}$$

$$\mathbf{M}_L = \begin{bmatrix} \mathbf{M}_{L1} \\ \mathbf{M}_{L2} \\ \vdots \\ \mathbf{M}_{d\mathcal{N}_{n_L}} \end{bmatrix}; \quad \mathbf{f}_L^{\text{ext}} = \begin{bmatrix} \mathbf{f}_{L1}^{\text{ext}} \\ \mathbf{f}_{L2}^{\text{ext}} \\ \vdots \\ \mathbf{f}_{d\mathcal{N}_{n_L}}^{\text{ext}} \end{bmatrix}; \quad \mathbf{f}_L^{\text{int}} = \begin{bmatrix} \mathbf{f}_{L1}^{\text{int}} \\ \mathbf{f}_{L2}^{\text{int}} \\ \vdots \\ \mathbf{f}_{d\mathcal{N}_{n_L}}^{\text{int}} \end{bmatrix} \tag{18}$$

with $\mathbf{f}_i^{\text{int}}, \mathbf{f}_i^{\text{ext}}, \mathbf{M}_i \in \mathbb{R}^{d\mathcal{N}_{n_i}}$.

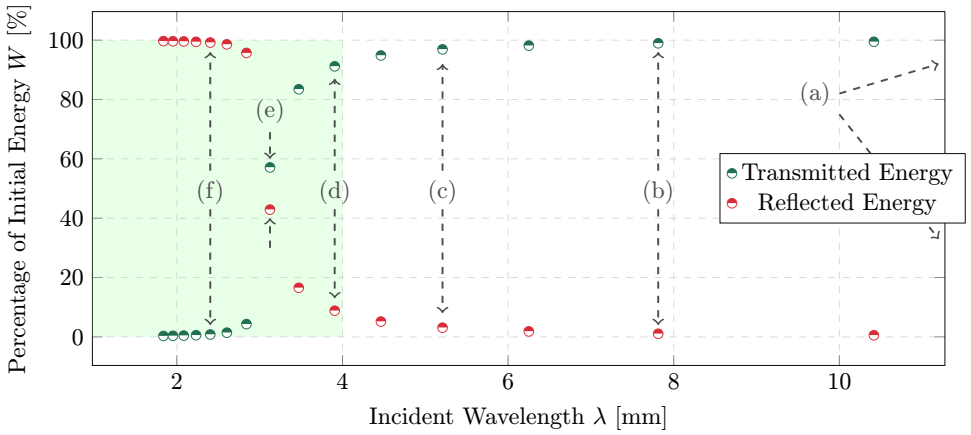

Fig. 4 Energy entrapment for 1D monochromatic spurious wave demonstration corresponding to Figs. 2 and 3 where the wavelength λ is varied in each simulation. The cut-off limit is determined by Nyquist-Shannon sampling theorem, where degradation of the solution is significant

2.3 Leapfrog time integration

To solve the body's motion through time t, each of the subdomains makes use of a symplectic integrator - the leapfrog scheme (also known as Verlet). At full time steps n, acceleration is explicitly solved for each Ω_i:

$$\ddot{\mathbf{u}}_i^n = \frac{(\mathbf{f}_i^{\text{ext}} - \mathbf{f}_i^{\text{int}})}{\mathbf{M}_i} \tag{19}$$

where the resulting vectorised quantities in Eqs. 17 - 18 eliminate the requirement of an inverted mass matrix. Computationally, this is advantageous. Subdomain velocities $\dot{\mathbf{u}}_i$ are solved in staggered fashion at the half time step $n + 1/2$:

$$\dot{\mathbf{u}}_i^{n+1/2} = \dot{\mathbf{u}}_i^{n-1/2} + \int_{t_i^{n-1/2}}^{t_i^{n+1/2}} \ddot{\mathbf{u}}_i \, dt \approx \dot{\mathbf{u}}_i^{n-1/2} + \ddot{\mathbf{u}}_i^n \Delta t_i \tag{20}$$

followed by the computation of displacements u, on at the next step $n + 1$:

$$\mathbf{u}_i^{n+1} = \mathbf{u}_i^n + \int_{t_i^n}^{t_i^{n+1}} \dot{\mathbf{u}}_i \, dt \approx \mathbf{u}_i^n + \dot{\mathbf{u}}_i^{n+1/2} \Delta t_i \tag{21}$$

Adjustment at the first time step $n = 0$, give velocities computed as:

$$\dot{\mathbf{u}}_i^{1/2} = \dot{\mathbf{u}}_i^0 + \ddot{\mathbf{u}}_i^0 \frac{\Delta t_i}{2} \tag{22}$$

where dimensions are consistent with $\ddot{\mathbf{u}}_i, \dot{\mathbf{u}}_i, \mathbf{u}_i \in \mathbb{R}^{d\mathcal{N}_{n_i}}$. This therefore provides the ingredients for the solution of each subdomain Ω_s and Ω_L. Through solving in parallel, continuity is enforced across the interface Γ of the two subdomains to give compatibility conditions:

$$\ddot{\mathbf{u}}_{\Gamma s}(\mathbf{C}_s \mathbf{x}_s) = \ddot{\mathbf{u}}_{\Gamma L}(\mathbf{C}_L \mathbf{x}_L) = \ddot{\mathbf{u}}_\Gamma(\mathbf{x}_\Gamma) \tag{23}$$

$$\mathbf{t}_{\Gamma s}(\mathbf{C}_s \mathbf{x}_s) = \mathbf{t}_{\Gamma L}(\mathbf{C}_L \mathbf{x}_L) = \mathbf{t}_\Gamma(\mathbf{x}_\Gamma) \tag{24}$$

where we denote $\mathbf{C}_s$ and $\mathbf{C}_L$ as boolean matrices that identify the subdomain degrees of freedom, for which $\mathbf{C}_L \mathbf{x}_L \in \Gamma_L$, $\mathbf{C}_s \mathbf{x}_s \in \Gamma_s$, and the intermediary interface $\mathbf{x}_\Gamma \in \Gamma$, to describe a common boundary between subdomains. While a comprehensive description of the coupling is reserved for Sect. 5, the immediate task is to describe the techniques for dissipating spurious reflections.

3 Methods of attenuation

In the following section we investigate the effectiveness of common attenuation methods in literature, combining their application with multi-time step integration and non-matching meshes in a coupled two-subdomain problem. Each of the methods are utilised during the time integration step, rather than as a post-processing tool, applied in space-time rather than frequency domain. We combine the methods of bulk viscosity, Soares Jnr's explicit dissipative integration scheme and the SPML method in a multi-time stepping framework [18, 24, 26]. These will serve as comparisons for the proposed method later in the paper.

3.1 Bulk viscosity method

Starting from the simplest method, application of bulk viscosity is a robust method, used to dissipate the energy present in high numerical frequencies [18].

$$\boldsymbol{\sigma}_{\text{d}} = \rho_i h_e (C_0 \text{Tr}\mathbf{D})^2 - C_1 c_e (\text{Tr}\mathbf{D}) \tag{25}$$

where ρ_i is the density of the subdomain, h_e the characteristic element length, c_e the dilatational wave speed, and (Tr$\mathbf{D}$) the trace of the rate of deformation. C_0 and C_1 are the quadratic and linear damping parameters, typically given as 1.44 and 0.06, respectively. Historically derived for shock conditions in hydrocodes by the aforementioned authors, the parameters are also called upon in other explicit simulations [18, 20, 35].

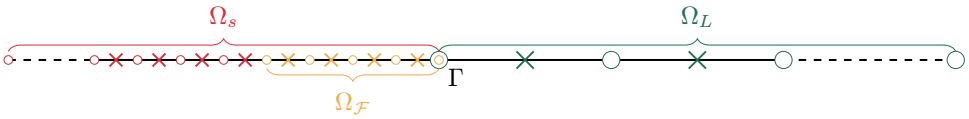

Fig. 5 In a 1D representation of a coupled domain, nodes are depicted as circles and crosses as Gauss integration points. Elements belonging to a filtering zone are a subset of the small subdomain $\Omega_{\mathcal{F}} \subset \Omega_s$ where the interface between the two is a singular point $\Gamma \in \Omega_{\mathcal{F}}$. Each element in $\Omega_{\mathcal{F}}$ requires the computation of σ_{d} at each cross

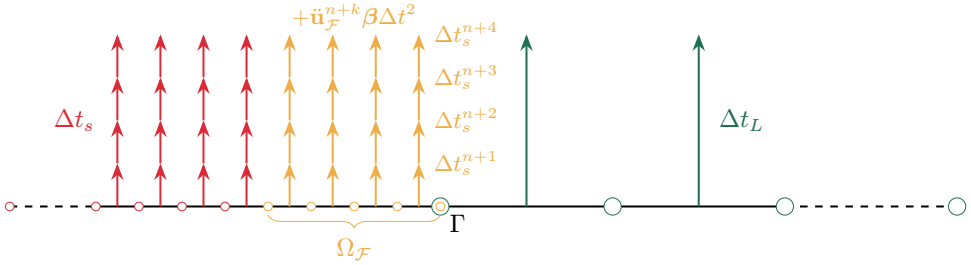

Fig. 6 In a coupled domain Ω_s and Ω_L are integrated with Δt_s and Δt_L. Elements within $\Omega_{\mathcal{F}}$ are also integrated over Δt_s, but also contain filtering control

Applying the $\boldsymbol{\sigma}_{\mathrm{d}}$ to a filtering zone $\Omega_{\mathcal{F}}$ of small nodes, the principle of virtual power in Ω_s is altered.

$$\delta P_s \approx \sum_{n=1}^{\mathcal{N}_{n_s}} \delta\dot{\mathbf{u}}_s \cdot (\mathbf{f}_s^{\mathrm{kin}} + \mathbf{f}_s^{\mathrm{int}} - \mathbf{f}_s^{\mathrm{ext}});$$
$$\text{where} \quad \mathbf{f}_s^{\mathrm{int}} = \int_{\Omega_s} \mathbf{B}_s^{\mathrm{T}}(\boldsymbol{\sigma}_s + \boldsymbol{\sigma}_{\mathcal{F}})\ \mathrm{d}\Omega \tag{26}$$

where accounting for the bulk viscosity term $\boldsymbol{\sigma}_{\mathcal{F}}$ can simply be added to the interpolation of the internal forces. Dimensions are consistent for both, where $\boldsymbol{\sigma}_{\mathcal{F}}$ simply contains zero for those elements not in $\Omega_{\mathcal{F}}$. As shown in Fig. 5, in the context of spurious wave reflection, bulk viscosity is applied to those integration points close to the interface between the two disparate meshes.

As Maheo et al. discusses, use of constant damping parameters prove to be a limitation in adapting to the spurious oscillations across multiple time steps [20]. Consequently, next we implement a dissipative time integration scheme, that adaptively dampens depending on the frequency of a spurious mode at a current point in time.

3.2 Dissipative time integration schemes

The following method of attenuation is within the class of time integration schemes with dissipation. Schemes combining multi-time step integration with dissipative control are still in their nascency. Kwon and Prakash recently developed the MTS-Bathe scheme to dissipate spurious oscillations in systems with stiff and flexible subdomains [36]. In this work, we combine another form of dissipative control as found in the works of Soares Jnr's explicit time integration method [24]. Thus, enabling a single step approach in a subdomain, adaptive dissipation is applied to the highest modes of the model without excessive algorithmic damping. As depicted in Fig. 6, Ω_s and Ω_L are integrated with the conventional leapfrog scheme in Eqs. 19 - 21, with time steps Δt_s and Δt_L, respectively. With the exception of a subset close to the interface Γ in $\Omega_{\mathcal{F}}$, where the scheme is combined with dissipative control.

In contrast to the aforementioned bulk viscosity, Soares proposed a method that varied dissipation across each degree of freedom through introducing β. For each Δt_s and at each degree of freedom a scalar β is computed as:

$$\beta = \min(\beta, \beta_{\max}, f_e); \quad \text{where} \quad \beta_{\max} = 1;$$
$$f_e = 2(1-\xi_e)/(\omega_e^{\max}\Delta t_s) \tag{27}$$

where a limit of $\beta_{\max}$ is imposed, with damping ratio ξ_e and maximum sampling frequency $\omega_e^{\max}$ of each element in $\Omega_{\mathcal{F}}$ being established. Considering the update of the displacements, Eq. 21 is adapted to:

$$\mathbf{u}_{\mathcal{F}}^{n+k} = \mathbf{u}_{\mathcal{F}}^{n+k} + \ddot{\mathbf{u}}_d^n \boldsymbol{\beta} \Delta t_s^2 \tag{28}$$

so long as oscillation is detected within a node, given a simple check of sign with respect to the previous time step $\dot{u}_{\mathcal{F}}^{n+1} \cdot \dot{u}_{\mathcal{F}}^{n} < 0$. Advantageously, the dissipative method is not an iterative process, unlike many of the aforementioned schemes. However, filtering in time introduces complexities in temporal accuracy and stability [37]. In addition, these dissipative schemes can unintentionally dampen the physical dynamics of the system, especially in wave-like PDEs [38]. For these reasons we now proceed to implement a targeted method for filtering in the spatial domain.

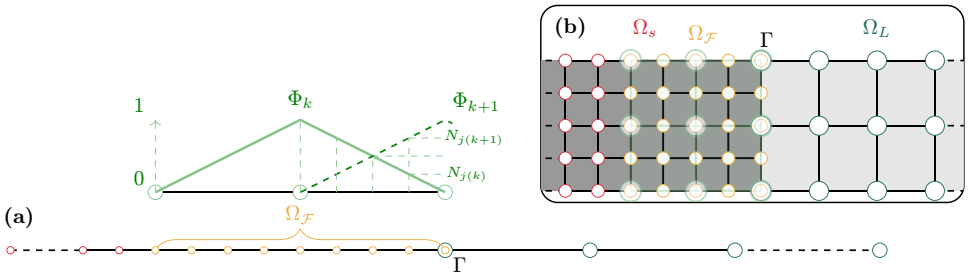

Fig. 7 Selective perfect matching layer (SPML) constructs an overlapping mesh in the small subdomain close to the coupled interface Γ; **a** the 1-D representation of $\Omega_{\mathcal{F}}$ with Lagrangian shape functions $\mathbf{\Phi}$ for each large overlapping node k at each small node j, **b** the 2-D representation of a simple bar where quadrilateral elements construct the mesh of $\Omega_{\mathcal{F}}$

3.3 Selective perfect matching layer

References to the classical PML are ubiquitous throughout numerical methods literature [39–41]. Marchais et al. addressed the incompatibility of non-uniform meshes by introducing a Selective PML (Perfectly Matched Layer). The approach specifically attenuates spurious frequencies, effectively separating them from issues caused by mesh incompatibilities [26]. The method requires two key fundamental building blocks. The first is the partitioning of the discretised dynamic fields, in this case the authors utilise displacements:

$$\mathbf{u}_s(t) : \mathbf{u}_{\mathcal{F}}(t) = \mathbf{u}_s(t) + \mathbf{u}_L(t) \quad \text{with} \quad \begin{cases} \mathbf{u}_s(t) = \mathbb{P}_s \mathbf{u}_{\mathcal{F}}(t) \\ \mathbf{u}_L(t) = \mathbb{Q}_L \mathbf{u}_{\mathcal{F}}(t) \end{cases} \tag{29}$$

where $\mathbb{P}_s$ and $\mathbb{Q}_L$ are the small and large field projection operators. Secondly, the modification of the PML allows for the automatic dissipation of just the small (high frequency) signal. In Fig. 7, a depiction of the a SPML filtering zone is depicted, both in the context of coupling a 1-D bar, but also 2-D.

Through definition of the overlapping region denoted $\Omega_{\mathcal{F}}$, the equation of motion in the filtering zone is given as:

$$\mathbf{M}_{\mathcal{F}} \ddot{\mathbf{u}}_{\mathcal{F}} + \mathbf{f}_{\mathcal{F}}^{\text{int}} - \mathbf{f}_{\mathcal{F}}^{\text{ext}} + 2\gamma_{\mathcal{F}} \mathbf{M} \mathbb{P}_s \dot{\mathbf{u}}_{\mathcal{F}} + \gamma_{\mathcal{F}}^2 \mathbf{M} \mathbb{P}_s \mathbf{u}_{\mathcal{F}} = \mathbf{0} \tag{30}$$

where $\gamma_{\mathcal{F}}$ is described as the filtering coefficient or damping factor. Grunwald et al. describe a clear minimum for this rate, optimal for spurious reflections [17]. Several constructions of the "microfield" projector can be described. Here we utilise the minimisation of the kinetic energy gap, with the features of the large shape functions:

$$\mathbb{P}_s = \mathbf{I} - \mathbb{N}_L \mathbf{M}_L^{-1} \mathbb{N}_L^{\mathrm{T}} \mathbf{M}_{\mathcal{F}} \tag{31}$$

given dimensions $\mathbb{P}_s \in \mathbb{R}^{d\mathcal{N}_{n_{\mathcal{F}}} \times d\mathcal{N}_{n_{\mathcal{F}}}}$ and $\mathbb{N}_L \in \mathbb{R}^{d\mathcal{N}_{n_{\mathcal{F}}} \times d\mathcal{N}_{n_{\mathcal{L}}}}$. Applying this additional contribution to $\Omega_{\mathcal{F}}$ constitutes a dissipative force:

$$\mathbf{f}_{\mathcal{F}} = \mathbf{M}_{\mathcal{F}} \ddot{\mathbf{u}}_{\mathcal{F}} = \mathbf{M}(2\gamma_{\mathcal{F}} \mathbb{P}_s \dot{\mathbf{u}}_{\mathcal{F}}(t) + \gamma_{\mathcal{F}}^2 \mathbb{P}_s \mathbf{u}_{\mathcal{F}}(t)) \tag{32}$$

applied at each Δt_s in the case of a multi-time stepping solution. Conveniently, this can also be applied as a damping acceleration $\ddot{\mathbf{u}}_d$ in a staggered scheme as:

$$\ddot{\mathbf{u}}_d^{n+1} = 2\gamma \mathbb{P}_s \dot{\mathbf{u}}_{\mathcal{F}}^{n-\frac{1}{2}} + \gamma^2 \mathbb{P}_s \mathbf{u}_{\mathcal{F}}^n \tag{33}$$

where the equivalent kinetic quantity will be denoted $\mathbf{f}_d^{\text{SPML}}$. The implications of utilising SPML lead to a change in the conditional stability where explicit time steps require Ω_s to integrate with:

$$\Delta t_{Cs} \leqslant \frac{2}{\sqrt{\omega^2_{(\mathcal{N}_{n_{\mathcal{F}}}+1)} + \gamma_{\mathcal{F}}^2}} \tag{34}$$

with $N_{n_{\mathcal{F}}}$ the number of elements in the filtering zone. Whilst effective, the SPML can be cumbersome to construct with an overlapping mesh of coincident nodes for which to filter upon.

In summary, this section has outlined three key dissipative methods for alleviating spurious wave reflection in a coupled dynamic domain. Whilst artificial viscosity is straightforward and a widely employed method, it is sensitive to material parameters and does not adapt to the frequency of the spurious wave. In comparison, the family of dissipative time integration schemes are adaptive through computing local time integration parameters that attenuate non-physical oscillations with full automation. Despite this, these methods are not specifically designed to target the unique problem of non-physical spurious reflections at interfaces between dynamically incompatible models or disparate meshes. SPML presents a more complex, but targeted solution to spurious wave reflection. Selective in its nature, filtering only incompatible waves makes it a good candidate for comparing the next generation of dissipative algorithms.

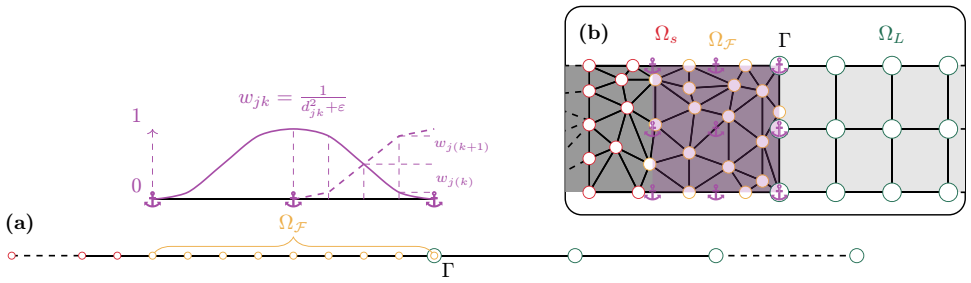

Fig. 8 Proposed Method with Shepard's Weights in $\Omega_{\mathcal{F}}$ where k denotes the large overlapping anchor points and j the small filtering node; **a** 1-D representation **b** 2-D representation

4 Proposed attenuation

In the following section we propose a new method of attenuation that looks to circumvent the limitations of aforementioned methods. We make a step forward in proposing an algorithm that targets the specific frequency of the mesh-induced spurious oscillations, whilst avoiding the construction of a mesh on the filtering region. The method is described in a dynamic setting, irrespective of subdomain geometries and is later combined with multi-time step integration and non-matching meshes.

4.1 Shepard-based projection method

Through the definition of an overlapping filtering region, as depicted in Fig. 8, we now outline the steps in constructing a new projector based on an inverse-distance weighting (IDW). Analogous to the construction of projection operators in the SPML, and the more recent weak staggered scheme, the proposed method looks to separate the kinematic contributions of the "unique" high frequency content with the "compatible" lower frequency [17, 26]. We maintain that the positions of the overlapping coarse discretisation remain consistent with Ω_L to target the high frequencies. However, rather than defining interpolation functions, Φ_L^k, from a finite element space, we utilise Shepard's definition of weights w_{jk} with [42]:

$$w_{jk} = \frac{1}{d_{jk}^p + \varepsilon}; \quad d_{jk} = \|\mathbf{x}_{\mathcal{F},j} - \mathbf{x}_{\mathcal{L},k}\|_2 \tag{35}$$

where the distance between each small position x_j in filter zone $\Omega_{\mathcal{F}}$ to every overlapping anchor point x_k (coarse discretisation) becomes the foundation of the new projection. A common usage of power $p = 2$ gives an inversely proportional weighting to the square of the distance, with $\epsilon = 1 \times 10^{-12}$ to avoid non-zero division. The distance matrix is of dimensions $\mathbf{d} \in \mathbb{R}^{d\mathcal{N}_{n_{\mathcal{F}}} \times d\mathcal{N}_{n_{\mathcal{L}}}}$ with the number of small filter nodes $\mathcal{N}_{n_{\mathcal{F}}}$ and large anchor points $\mathcal{N}_{n_{\mathcal{L}}}$. The weights are assembled into matrix $\mathbb{N}_{\mathcal{L}}$ as:

$$\mathbb{N}_{\mathcal{L},jk} = \begin{cases} \frac{w_{jk}}{\sum_{k\in\mathcal{N}_j} w_{jk}} & k \in \mathcal{N}_j \\ 0 & \text{otherwise} \end{cases} \tag{36}$$

where for each small filter node j, we normalise over its k nearest coarse neighbour in the large anchor set $\mathcal{N}_j$. We observe $\mathbb{N}_{\mathcal{L}}$ shares the same dimensions as $\mathbf{d}$. To compute the inertial contribution of this dissipating force, the lumped mass vector of the overlapping anchors $\mathbf{m}_{\mathcal{L}}$ must be found:

$$\mathbf{m}_{\mathcal{L}} = (\mathbb{N}_{\mathcal{L}} \circ \mathbb{N}_{\mathcal{L}})^T \mathbf{m}_{\mathcal{F}} \equiv \left(\mathbb{N}_{\mathcal{L}}^{\circ 2}\right)^T \mathbf{m}_{\mathcal{F}} \tag{37}$$

where $(\cdot)^{\circ 2}$ is the Hadamard power signifying the element-wise power and $\mathbf{m}_{\mathcal{F}}$ the mass of the small nodes in the filtering zone. Construction of the anchor masses allows for a mass-normalised projection term to be used in the microfield projector:

$$\check{\mathbb{N}}_{\mathcal{L}}^T = \text{diag}(\mathbf{m}_{\mathcal{L}})^{-1} \mathbb{N}_{\mathcal{L}}^T \text{diag}(\mathbf{m}_{\mathcal{F}}); \quad \check{N}_{\mathcal{L},kj} = N_{\mathcal{L},jk} \frac{m_{\mathcal{F},j}}{m_{\mathcal{L},k}} \tag{38}$$

however as $\mathbf{m}_{\mathcal{L}}$ and $\mathbf{m}_{\mathcal{F}}$ are vectors, these are implemented efficiently as element-wise operations, rather than requiring the inverse of weights matrix. Applying the projection to obtain the damping acceleration in the filter zone gives:

$$\ddot{\mathbf{u}}_d = -2\gamma_{\mathcal{F}} \mathbb{P}_s \dot{\mathbf{u}}_s - \gamma_{\mathcal{F}}^2 \mathbb{P}_s \mathbf{u}_s \tag{39}$$

where $\ddot{\mathbf{u}}_d \in \mathbb{R}^{d\mathcal{N}_{n_{\mathcal{F}}} \times 1}$, and $\gamma_{\mathcal{F}}$ remains the filtering coefficient defined in the SPML. Applying the projection to velocity and displacement contains the mass-normalised weights:

$$\mathbb{P}_s \dot{\mathbf{u}}_s = \dot{\mathbf{u}}_s - \mathbb{N}_{\mathcal{L}} \left(\check{\mathbb{N}}_{\mathcal{L}}^{\mathrm{T}} \dot{\mathbf{u}}_s\right); \quad \mathbb{P}_s \mathbf{u}_s = \mathbf{u}_s - \mathbb{N}_{\mathcal{L}} \left(\check{\mathbb{N}}_{\mathcal{L}}^{\mathrm{T}} \mathbf{u}_s\right) \tag{40}$$

Subsequently, such a projection allows for damping to be applied to the subdomain's global nodal vectors, at each Δt_s, as an acceleration or equivalent internal force:

$$\mathbf{f}_s^{\text{int}} \leftarrow \mathbf{f}_s^{\text{int}} - \text{diag}(\mathbf{m}_{\mathcal{F}}) \ddot{\mathbf{u}}_d \tag{41}$$

4.2 Algorithmic representation of the method

Figure 8 part (b) illustrates how the overlapping region, need not require the construction of a mesh where nodes are coin-

cident with the underlying Ω_s mesh. Omitting the need for storing connectivity, a scattered set of large anchor points can be used to project in $\Omega_{\mathcal{F}}$. The method is summarised in Algorithm 1.

Algorithm 1 Spurious Wave Attenuation via Shepard-Based Projection

Require: Small filter positions $\mathbf{x}_{\mathcal{F}}$, velocities $\dot{\mathbf{u}}_{\mathcal{F}}$, overlapping large anchor positions $\mathbf{x}_{\mathcal{L}}$, velocities $\dot{\mathbf{u}}_L$, filtering coefficient $\boldsymbol{\gamma}_{\mathcal{F}}$, power p, nearest neighbour k in $\Omega_{\mathcal{F}}$

Ensure: Updated small velocities $\dot{\mathbf{u}}_s$ and displacements $\mathbf{u}_s$ with attenuation

$\mathcal{N}_{n_{\mathcal{F}}}, \mathcal{N}_{n_{\mathcal{L}}} \leftarrow \text{len}(\mathbf{x}_{\mathcal{F}}), \text{len}(\mathbf{x}_{\mathcal{L}})$

Compute distance matrix: $\mathbf{d} = \|\mathbf{x}_{\mathcal{F}}^{(j)} - \mathbf{x}_{\mathcal{L}}^{(k)}\|_2, \; j = 1, \ldots, \mathcal{N}_{n_{\mathcal{F}}}, \; k = 1, \ldots, \mathcal{N}_{n_{\mathcal{L}}}$

Compute inverse weights: $\mathbf{w}(j) = (\mathbf{d}^p + \epsilon)^{-1}$ for $j \in \mathcal{N}_k(j)$

Find k nearest neighbours: $\mathcal{N}_k(j) \leftarrow$ `argpartition(`$\mathbf{d}[j, :], k-1)[:k]$

for $j = 1$ to $\mathcal{N}_{\mathcal{F}}$ **do**

  if any $d_j = 0 + \epsilon$ **then**

    $\mathbb{N}_{\mathcal{L}}[j, k] = 1.0$

  else

    Normalise $\mathbb{N}_{\mathcal{L}}[j, k] = w_{jk} / \sum_{j \in \mathcal{N}_k(j)} w_{jk}$ for $j \in \mathcal{N}_k(j)$

  end if

end for

Compute lumped anchor masses: $\mathbf{m}_{\mathcal{L}} = \left(\mathbb{N}_{\mathcal{L}}^{\circ 2}\right)^T \mathbf{m}_{\mathcal{F}}$

Compute mass-normalised weight matrix: $\check{\mathbb{N}}_{\mathcal{L}}^T = \text{diag}(\mathbf{m}_{\mathcal{L}})^{-1} \mathbb{N}_{\mathcal{L}}^T \text{diag}(\mathbf{m}_{\mathcal{F}})$

Apply projection: $\mathbb{P}_s \dot{\mathbf{u}}_s = \dot{\mathbf{u}}_s - \mathbb{N}_{\mathcal{L}} \left(\tilde{\mathbb{N}}_{\mathcal{L}}^{\mathrm{T}} \dot{\mathbf{u}}_s\right); \quad \mathbb{P}_s \mathbf{u}_s = \mathbf{u}_s - \mathbb{N}_{\mathcal{L}} \left(\tilde{\mathbb{N}}_{\mathcal{L}}^{\mathrm{T}} \mathbf{u}_s\right)$

Compute damping acceleration: $\ddot{\mathbf{u}}_d = 2\gamma_{\mathcal{F}} \mathbb{P}_s \dot{\mathbf{u}}_s + \gamma_{\mathcal{F}}^2 \mathbb{P}_s \mathbf{u}_s$

Update filtered internal forces: $\mathbf{f}_s^{\text{int}} \leftarrow \mathbf{f}_s^{\text{int}} - \text{diag}(\mathbf{m}_{\mathcal{F}}) \ddot{\mathbf{u}}_d$

Algorithmically, rather than computing a dense IDW kernel matrix, the k-nearest neighbours (k-NN) algorithm is utilised to limit the calculation of weights to just the nearest large anchor points [43]. Computation of these distances and weights between filtering nodes $\mathbf{x}_{\mathcal{F}}$ to scattered large points $\mathbf{x}_{\mathcal{L}}$, and sorting of the nearest neighbours contribute most significantly to the complexity of the algorithm. Relative to the proposed method, bulk viscosity and the dissipative time integration method described are computationally cheaper. While these methods scale with the number of elements in the filtering region as $\mathcal{O}(\mathcal{N}_{n_{\mathcal{F}}})$, the Shepard-based method is more expensive as it filters with an overlapping region to give $\mathcal{O}(\mathcal{N}_{n_{\mathcal{F}}} \cdot \mathcal{N}_{n_{\mathcal{L}}})$. However, this cost remains less than the dense projection seen in the SPML method with quadratic scaling $\mathcal{O}(\mathcal{N}_{n_{\mathcal{F}}}^2)$. Despite the proposed method requiring an additional cost to its simpler predecessors, the following sections will look to show the improvement in dissipation over the spectrum of incompatible frequencies. In addition, we will show a direct coupling of subdomains, that avoids the iterative solution of a system of equations. Algorithm 1 outlines how these computations are declared prior to the loop over the filtering nodes to reduce computational expense.

While attenuation methods are applicable to uncoupled systems, their application to coupled subdomains is where significant advancements are made [44]. In addition, for 2-D and 3-D problems, non-matching meshes also arise. We therefore present modifications to both spatial and temporal finite element coupling algorithms that combine the aforementioned attenuation to mitigate spurious wave reflection.

5 Applying attenuation within coupled schemes

In the following section, we detail the finite element coupling method for subdomains with non-conforming interfaces. This method, calls upon recent work that permits each subdomain to be solved with its own independent time step [44, 45]. Subsequently, we look to address the compatibility of Eq. 23, whilst suppressing spurious waves. While the method shares familiarities with generic Lagrange multiplier techniques, this work highlights its notable differences.

5.1 Coupling non-matching meshes with multi-time stepping

In the current coupling, we look for an efficient approach in projecting kinematic quantities from non-matching subdomains to an external interface. One that computes a coarse-field approximation of acceleration, solving explicitly rather than by solving a system of equations. Here we denote this interface as Γ, and subsequently discretise with finite elements:

$$\dot{\mathbf{u}}_\Gamma(\mathbf{x}, t) \approx \sum_{i=1}^{\mathcal{N}_n} N_i(x_\Gamma) \dot{u}_\Gamma(t) = \mathbf{N}_\Gamma(\mathbf{x}_\Gamma) \dot{\mathbf{u}}_\Gamma(t) \tag{42}$$

The choice of interface interpolation functions are Lagrangian shape functions, with a linear isoparametric mapping, stored within the following operators:

$$\mathbf{N}_s \in \mathbb{R}^{d\mathcal{N}_{\Gamma s} \times d\mathcal{N}_\Gamma} \quad \mathbf{N}_L \in \mathbb{R}^{d\mathcal{N}_{\Gamma L} \times d\mathcal{N}_\Gamma} \tag{43}$$

where $(\cdot)^d$ is dimension, $\mathcal{N}_{\Gamma s}$ and $\mathcal{N}_{\Gamma L}$ are the number of nodes on the interfaces of the small and large subdomain, and $\mathcal{N}_\Gamma$ the number on externally assembled Γ. The projection on the small subdomain's interface $\mathbf{N}_s$ necessitates the computation of the shape functions, whereas a one-to-one mapping simplifies $\mathbf{N}_L$ to an identity matrix. To satisfy the principle of virtual power, whilst accounting for the contributions of the coupling interface gives:

$$\delta P = \delta P_s + \delta P_L + \delta P_\Gamma$$

$$
\begin{aligned}
&= \delta\dot{\mathbf{u}}_s^{\mathrm{T}}\{\mathbf{f}_s^{\mathrm{int}} - \mathbf{f}_s^{\mathrm{ext}} + \mathbf{M}_s\ddot{\mathbf{u}}_s + \mathbf{N}_s^{\mathrm{T}}\mathbf{f}_{\Gamma s}\} \\
&\quad + \delta\dot{\mathbf{u}}_L^{\mathrm{T}}\{\mathbf{f}_L^{\mathrm{int}} - \mathbf{f}_L^{\mathrm{ext}} + \mathbf{M}_L\ddot{\mathbf{u}}_L + \mathbf{N}_L^{\mathrm{T}}\mathbf{f}_{\Gamma L}\} \\
&\quad + \delta\mathbf{f}_{\Gamma s}^{\mathrm{T}}\{\mathbf{N}_s^{\mathrm{T}}\dot{\mathbf{u}}_{\Gamma s} - \mathbf{L}_s^{\mathrm{T}}\dot{\mathbf{u}}_{\Gamma}\} + \delta\mathbf{f}_{\Gamma L}^{\mathrm{T}}\{\mathbf{N}_L^{\mathrm{T}}\dot{\mathbf{u}}_{\Gamma L} - \mathbf{L}_L^{\mathrm{T}}\dot{\mathbf{u}}_{\Gamma}\} \\
&\quad - \delta\dot{\mathbf{u}}_{\Gamma}^{\mathrm{T}}\{\mathbf{N}_L^{\mathrm{T}}\mathbf{f}_{\Gamma L} + \mathbf{N}_s^{\mathrm{T}}\mathbf{f}_{\Gamma s}\} \qquad (44)
\end{aligned}
$$

where damping within the filtering zone is incorporated within the virtual power of Ω_s and the internal forces. Expressed in virtual power terms obtains $\delta P_{\mathcal{F}} = \delta\dot{\mathbf{u}}_{\mathcal{F}}^{\mathrm{T}}\{\mathbf{M}_{\mathcal{F}}\ddot{\mathbf{u}}_d\}$. For each subdomain Ω_i, it is convenient to define $\mathbf{N}_i^{\mathrm{T}} = \mathbf{R}_i$, to resolve the behaviour of the interface. Subsequently, the direct solution requires the summation of the following:

$$\mathbf{M}_{\Gamma} = \mathbf{R}_s\mathbf{C}_s^{\mathrm{T}}\mathbf{M}_s + \mathbf{R}_L\mathbf{C}_L^{\mathrm{T}}\mathbf{M}_L = \mathbf{R}_s\mathbf{M}_{\Gamma s} + \mathbf{R}_L\mathbf{M}_{\Gamma L} \qquad (45)$$

$$\mathbf{f}_{\Gamma}^{\mathrm{int}} = \mathbf{R}_s\mathbf{C}_s^{\mathrm{T}}\mathbf{f}_s^{\mathrm{int}} + \mathbf{R}_L\mathbf{C}_L^{\mathrm{T}}\mathbf{f}_L^{\mathrm{int}} = \mathbf{R}_s\mathbf{f}_{\Gamma s}^{\mathrm{int}} + \mathbf{R}_L\mathbf{f}_{\Gamma L}^{\mathrm{int}} \qquad (46)$$

$$\mathbf{f}_{\Gamma}^{\mathrm{ext}} = \mathbf{R}_s\mathbf{C}_s^{\mathrm{T}}\mathbf{f}_s^{\mathrm{ext}} + \mathbf{R}_L\mathbf{C}_L^{\mathrm{T}}\mathbf{f}_L^{\mathrm{ext}} = \mathbf{R}_s\mathbf{f}_{\Gamma s}^{\mathrm{ext}} + \mathbf{R}_L\mathbf{f}_{\Gamma L}^{\mathrm{ext}} \qquad (47)$$

where attenuation is accounted for in $\mathbf{f}_s^{\mathrm{int}}$. Through isolation of the interface problem, computation of the kinematic condition on each subdomain can be computed with a mapping back from Γ onto the subdomains:

$$\ddot{\mathbf{u}}_{\Gamma} = \frac{(\mathbf{f}_{\Gamma}^{\mathrm{ext}} - \mathbf{f}_{\Gamma}^{\mathrm{int}})}{\mathbf{M}_{\Gamma}}; \quad \ddot{\mathbf{u}}_{\Gamma s} = \mathbf{N}_s\ddot{\mathbf{u}}_{\Gamma}; \quad \ddot{\mathbf{u}}_{\Gamma L} = \mathbf{N}_L\ddot{\mathbf{u}}_{\Gamma} \qquad (48)$$

Consequently, the issue of non-matching meshes is solved with a mapping of masses and forces onto Γ, and accelerations back onto the subdomain interfaces Γ_s and Γ_L. Next we will consider leveraging the solution of subdomains with their own time steps. At each Δt_L, Eqs. 45 - 47 are computed, followed by Eq. 48, enforcing a constant acceleration across the large step.

To enable a more efficient solution, elements must be integrated as close to the stability limit as possible, defined by the Courant-Friedrichs-Lewy condition [46], with those in the filtering zone requiring a more stringent condition [26]:

$$\Delta t_C = \frac{2}{\omega_C} \leq \min_e\left(\frac{h_e}{c_e}\right); \quad \Delta t_{\mathcal{F}} \leqslant \frac{2}{\sqrt{\omega^2_{(\mathcal{N}_{n_{\mathcal{F}}}+1)} + \max\{\boldsymbol{\gamma}_{\mathcal{F}}\}^2}} \qquad (49)$$

where for element e, characteristic length h_e and c_e may vary between subdomain. Marchais et al. have shown the stability criterion for central difference based methods to require the filtering coefficient γ [26]. Granted the CFL condition in small and large subdomain may vary, we introduce time steps Δt_{Cs} and Δt_{CL}, respectively.

A very brief overview of the multi-time stepping algorithm used is introduced here. To determine the number of small steps that can proceed for every large step, the trial step t_{Ti} is computed as:

$$t_{Ts}^{n+k} = \min\{t_s + \Delta t_{Cs}, t_s + \Delta t_{\mathcal{F}}\}; \quad t_{TL}^{N+1} = t_L + \Delta t_{CL} \qquad (50)$$

where n denotes the small and N the large subdomain's step, respectively. Subsequently, assuming $\Delta t_s \neq \Delta t_L$, a simple ratio is computed to determine the integration steps. The algorithm ensures the integration of Ω_s first, followed by the calculation of the next time step ratio $t_{\mathrm{ratio}}^{n+k+1}$:

$$t_{\mathrm{ratio}}^{n+k+1} = \frac{(t_s^{n+k} + \Delta t_s^{n+k}) - t_L^N}{t_{TL}^{N+1} - t_L^N} \qquad (51)$$

checking for the condition $t_{\mathrm{ratio}}^{n+k+1} \leq 1$ before Ω_L is integrated in time. To guarantee Ω_s and Ω_L find common time steps, each large step is synchronised with parameter α:

$$t_L^{N+1} = t_s^{n+k} = \begin{cases} t_s^n + \sum_{k=0}^{k-1}\Delta t_{Cs}^{n+k} + \alpha_s \cdot \Delta t_{Cs}^{n+k}, & \alpha_s > \alpha_L \\ t_s^n + \alpha_L \cdot \Delta t_{CL}^N, & \alpha_L \geq \alpha_s \end{cases} \qquad (52)$$

where α_s and α_L reduce the time step on Ω_s and Ω_L, respectively. This ensures that at least one of the subdomains always steps with the largest stable time step possible. Large ratios of $m > 10$, are particularly challenging when ensuring numerical stability, in these cases the remedy of moving the interface Γ one element into Ω_s has been previously suggested. For further details on the integration procedure with multiple time steps the reader is referred to the following work [45]. The combination with coupling operators that enable non-matching meshes can also be found by the authors [44]. In this work the coupling is advanced to attenuate spurious wave reflections.

5.2 Coupling strategies with Lagrange multipliers

The localised Lagrange multiplier (LLM) method is a well established approach for the construction of an external frame (interface) to couple non-matching subdomains [47, 48]. The most recent improvements look to also combine multiple time steps, as well as the automatic solution of the reduced basis on the interface [49–52]. The following outlines the steps in coupling localised Lagrange multipliers with the aforementioned SPML, as a means to compare against the proposed approach. The undamped system can be written as:

$$\begin{bmatrix} \mathbf{M}_s & 0 & \mathbf{C}_s\mathbf{A}_s^{\mathrm{T}} & 0 & 0 \\ 0 & \mathbf{M}_L & 0 & \mathbf{C}_L\mathbf{A}_L^{\mathrm{T}} & 0 \\ \mathbf{A}_s\mathbf{C}_s^{\mathrm{T}} & 0 & 0 & 0 & -\mathbf{L}_s \\ 0 & \mathbf{A}_L\mathbf{C}_L^{\mathrm{T}} & 0 & 0 & -\mathbf{L}_L \\ 0 & 0 & -\mathbf{L}_s^{\mathrm{T}} & -\mathbf{L}_L^{\mathrm{T}} & 0 \end{bmatrix} \begin{bmatrix} \ddot{\mathbf{u}}_s \\ \ddot{\mathbf{u}}_L \\ \boldsymbol{\lambda}_s \\ \boldsymbol{\lambda}_L \\ \ddot{\mathbf{u}}_{\Gamma} \end{bmatrix} = \begin{bmatrix} \mathbf{f}_s^{\mathrm{ext}} - \mathbf{f}_s^{\mathrm{int}} \\ \mathbf{f}_L^{\mathrm{ext}} - \mathbf{f}_L^{\mathrm{int}} \\ 0 \\ 0 \\ 0 \end{bmatrix} \qquad (53)$$

where for the case of coupling with Lagrange multipliers, mass is commonly presented as matrix $\mathbf{M}_i \in \mathbb{R}^{d\mathcal{N}_{n_i} \times d\mathcal{N}_{n_i}}$ rather than its vectorised counterpart. Coupling operators $\mathbf{C}_i \in \mathbb{R}^{d\mathcal{N}_{\Gamma i} \times d\mathcal{N}_{n_i}}$ extract the subdomain boundary accelerations, $\mathbf{A}_i \in \mathbb{R}^{d\mathcal{N}_{\Gamma i} \times d\mathcal{N}_{\Gamma i}}$ project these degrees of freedom onto the interface frame and $\mathbf{L}_i \in \mathbb{R}^{d\mathcal{N}_{\Gamma i} \times d\mathcal{N}_{\Gamma}}$ interpolates from the frame back to the subdomains' boundary.

$$\mathbf{A}_s = \int_{\Gamma_s} \mathbf{N}_{\ddot{u}_s}^{\mathrm{T}} \mathbf{N}_{\lambda_s} \, \mathrm{d}\Gamma; \quad \mathbf{A}_L = \int_{\Gamma_L} \mathbf{N}_{\ddot{u}_L}^{\mathrm{T}} \mathbf{N}_{\lambda_L} \, \mathrm{d}\Gamma \tag{54}$$

$$\mathbf{L}_s = \int_{\Gamma_s} \mathbf{N}_{\lambda_s}^{\mathrm{T}} \mathbf{N}_{\ddot{u}\Gamma} \, \mathrm{d}\Gamma; \quad \mathbf{L}_L = \int_{\Gamma_L} \mathbf{N}_{\lambda_L}^{\mathrm{T}} \mathbf{N}_{\ddot{u}\Gamma} \, \mathrm{d}\Gamma \tag{55}$$

where localised Lagrange multiplier frame provides additional flexibility compared to rigid mortar constraints, allowing $\ddot{\mathbf{u}}_\Gamma$ to be approximated with its own discretisation. This study uses the classical form where $\mathbf{A}_i = \mathbf{I}$ and $\mathbf{L}_i$ utilises the conventional first order Lagrangian shape functions, however for optimised forms of the coupling operators the reader is referred to the works of Dvořák and González [51]. Attenuation of the spurious waves is applied, prior to the solution of the interface:

$$\tilde{\ddot{\mathbf{u}}}_s = \mathbf{M}_s^{-1}(\mathbf{f}_s^{\mathrm{ext}} - \mathbf{f}_s^{\mathrm{int}} - \mathbf{f}_d^{\mathrm{SPML}}); \quad \tilde{\ddot{\mathbf{u}}}_L = \mathbf{M}_L^{-1}(\mathbf{f}_L^{\mathrm{ext}} - \mathbf{f}_L^{\mathrm{int}}) \tag{56}$$

where $\tilde{\ddot{\mathbf{u}}}_i$ is referred to as the unconstrained acceleration (without coupling) of Ω_i. Dissipative term $\mathbf{f}_d^{\mathrm{SPML}}$ corresponds to the damping field $\ddot{\mathbf{u}}_d$ in Eq. 33. Continuity is enforced with equal and opposite forces $\mathbf{L}_s^{\mathrm{T}}\boldsymbol{\lambda}_s = -\mathbf{L}_L^{\mathrm{T}}\boldsymbol{\lambda}_L$ at common time steps, to give the constrained accelerations in the final form:

$$\ddot{\mathbf{u}}_s = \tilde{\ddot{\mathbf{u}}}_s - \mathbf{M}_s^{-1}(\mathbf{A}_s\mathbf{C}_s^{\mathrm{T}}\boldsymbol{\lambda}_s); \quad \ddot{\mathbf{u}}_L = \tilde{\ddot{\mathbf{u}}}_L - \mathbf{M}_L^{-1}(\mathbf{A}_L\mathbf{C}_L^{\mathrm{T}}\boldsymbol{\lambda}_L) \tag{57}$$

For integration in time, this work combines the SPML dissipation with the CDM-based multi-time step integration method in the works of Cho et al. [53]. The method assumes an integer ratio m between Δt_L and Δt_s, solving at each Δt_s, the system of equations on the interface:

$$\begin{bmatrix} \mathbf{A}_s(\mathbf{C}_s^{\mathrm{T}}\mathbf{M}_s^{-1}\mathbf{C}_s)\mathbf{A}_s^{\mathrm{T}} & 0 & -\mathbf{L}_s^{\mathrm{T}} \\ 0 & \mathbf{A}_L(\mathbf{C}_L^{\mathrm{T}}\mathbf{M}_L^{-1}\mathbf{C}_L)\mathbf{A}_L^{\mathrm{T}} & -\mathbf{L}_L^{\mathrm{T}} \\ -\mathbf{L}_s^{\mathrm{T}} & -\mathbf{L}_L^{\mathrm{T}} & 0 \end{bmatrix} \begin{bmatrix} \boldsymbol{\lambda}_s \\ \boldsymbol{\lambda}_L \\ \ddot{\mathbf{u}}_\Gamma \end{bmatrix} = \begin{bmatrix} \mathbf{A}_s\mathbf{C}_s^{\mathrm{T}}\tilde{\ddot{\mathbf{u}}}_s \\ \mathbf{A}_L\mathbf{C}_L^{\mathrm{T}}\tilde{\ddot{\mathbf{u}}}_L \\ 0 \end{bmatrix} \tag{58}$$

where an increase in computational overhead is evident from the solution at each step. The inversion of mass matrices is a key topic of interest, for which direct solutions have been described by similar authors [54, 55]. This overview elucidates the core of the aforementioned coupling in Sect. 5.1. Thus, the proposed coupling can be viewed as a select case of the localised Lagrange multipliers, where the frame quantities are restricted to the coarse discretisation of the interface and solved explicitly. In Algorithms 2 and 3 we summarise the proposed algorithm using the Shepard-based projection and the localised Lagrange Multiplier coupling with the SPML for comparison. Whilst the Lagrange multiplier coupling solves a system of equations on the interface, the proposed method directly solves its kinematic and kinetics. It also allows for non-integer time step ratios between small and large subdomains, enabled through computation of the time step ratios.

Algorithm 2 Explicit Coupling with Shepard-Based Projection Method

procedure PROPOSED STEP
  while $t_{\mathrm{ratio}}^{n+k+1} \leq 1$ **do**
    Solve Explicitly $\ddot{\mathbf{u}}_{\Gamma_s}$ and $\mathbf{N}_s$
    Integrate Ω_s with $\ddot{\mathbf{u}}_{\Gamma_s}$
    Apply $\mathrm{diag}(\mathbf{m}_{\mathcal{F}})\ddot{\mathbf{u}}_d$ to $\mathbf{f}_s^{\mathrm{int}}$
    Assemble $\mathbf{f}_s^{\mathrm{int}}$, $\mathbf{f}_s^{\mathrm{ext}}$
    Compute t_{Ts}^{n+k}, t_{TL}^{N+1}, $t_{\mathrm{ratio}}^{n+k+1}$
  end while
  if $\alpha_L > \alpha_s$ **then**
    $\Delta t_L = \alpha_L \cdot \Delta t_L$
  else
    $\Delta t_s = \alpha_s \cdot \Delta t_s$
    Solve Explicitly $\ddot{\mathbf{u}}_{\Gamma_s}$ and $\mathbf{N}_s$
    Integrate Ω_s with $\ddot{\mathbf{u}}_{\Gamma_s}$
    Apply $\mathrm{diag}(\mathbf{m}_{\mathcal{F}})\ddot{\mathbf{u}}_d$ to $\mathbf{f}_s^{\mathrm{int}}$
    Assemble $\mathbf{f}_s^{\mathrm{int}}$, $\mathbf{f}_s^{\mathrm{ext}}$
    Compute t_{Ts}^{n+k}, t_{TL}^{N+1}, $t_{\mathrm{ratio}}^{n+k+1}$
  end if
  Solve Explicitly $\ddot{\mathbf{u}}_{\Gamma_L}$ and $\mathbf{N}_L$
  Integrate Ω_L with $\ddot{\mathbf{u}}_{\Gamma_L}$
  Assemble $\mathbf{f}_L^{\mathrm{int}}$, $\mathbf{f}_L^{\mathrm{ext}}$
  Assemble $\mathbf{M}_\Gamma$, $\mathbf{f}_\Gamma^{\mathrm{int}}$ and $\mathbf{f}_\Gamma^{\mathrm{ext}}$
  Compute t_{Ts}^{n+k}, t_{TL}^{N+1}, $t_{\mathrm{ratio}}^{n+k+1}$
end procedure

5.3 Effects of attenuation on coupled energy balance

Following aforementioned works assessing the stability of systems with multiple time steps, we analyse the proposed method from an energy perspective [56, 57]. The total amount of work done, or the energy transferred, at discrete time intervals for the coupled system can be written as:

$$W_s^{\mathrm{ext}} - W_s^{\mathrm{int}} - W_s^{\mathrm{kin}} + W_L^{\mathrm{ext}} - W_L^{\mathrm{int}} - W_L^{\mathrm{kin}} = W_s^{\mathrm{link}} + W_L^{\mathrm{link}} \tag{59}$$

Algorithm 3 Lagrange Multiplier Coupling with SPML Method

procedure LOCALISED LM STEP
  $m = \Delta t_L / \Delta t_s$
  while $k \leq m$ **do**
    Compute Unconstrained $\tilde{\ddot{\mathbf{u}}}_s$, $\tilde{\ddot{\mathbf{u}}}_L$
    Apply SPML with $\ddot{\mathbf{u}}_d$ to $\tilde{\mathbf{R}}_s$
    Assemble Interface System $\mathbf{C}_s^{\mathrm{T}}\mathbf{M}_s^{-1}\mathbf{C}_s$, $\mathbf{C}_L^{\mathrm{T}}\mathbf{M}_L^{-1}\mathbf{C}_L$, $\mathbf{A}_L$, $\mathbf{A}_s$, $\mathbf{L}_L^{\mathrm{T}}$ and $\mathbf{L}_s^{\mathrm{T}}$
    Solve Interface System of Equations for $\boldsymbol{\lambda}_L$, $\boldsymbol{\lambda}_s$, $\ddot{\mathbf{u}}_\Gamma$
    Compute Constrained $\ddot{\mathbf{u}}_s$
    Integrate Ω_s with $\ddot{\mathbf{u}}_\Gamma$
    Update frame $\dot{\mathbf{u}}_\Gamma$, $\mathbf{u}_\Gamma$
    Assemble $\mathbf{f}_s^{\mathrm{int}}$, $\mathbf{f}_s^{\mathrm{ext}}$
    Increment counter k
  end while
  Solve System for $\tilde{\ddot{\mathbf{u}}}_L$
  Compute Constrained $\ddot{\mathbf{u}}_L$
  Integrate Ω_L with $\ddot{\mathbf{u}}_\Gamma$
  Enforce continuity with frame $\dot{\mathbf{u}}_\Gamma$, $\mathbf{u}_\Gamma$ to avoid drifting
  Assemble $\mathbf{f}_L^{\mathrm{int}}$, $\mathbf{f}_L^{\mathrm{ext}}$
  Reset counter k
end procedure

where W_i^{ext}, W_i^{int} and W_i^{kin} denote external, internal and kinetic work components for subdomain Ω_i. Each of the subdomain components can be written with the respective global vectors as:

$$W_s^{\mathrm{int}} = \frac{1}{2}\mathbf{u}_s^{\mathrm{T}}(\mathbf{f}_s^{\mathrm{int}}); \quad W_s^{\mathrm{ext}} = \frac{1}{2}\mathbf{u}_s^{\mathrm{T}}(\mathbf{f}_s^{\mathrm{ext}});$$
$$W_s^{\mathrm{kin}} = \frac{1}{2}(\dot{\mathbf{u}}_s)^{\mathrm{T}}\mathrm{diag}(\mathbf{M})\dot{\mathbf{u}}_s \tag{60}$$

$$W_L^{\mathrm{int}} = \frac{1}{2}\mathbf{u}_L^{\mathrm{T}}(\mathbf{f}_L^{\mathrm{int}}); \quad W_L^{\mathrm{ext}} = \frac{1}{2}\mathbf{u}_L^{\mathrm{T}}(\mathbf{f}_L^{\mathrm{ext}});$$
$$W_L^{\mathrm{kin}} = \frac{1}{2}(\dot{\mathbf{u}}_L)^{\mathrm{T}}\mathrm{diag}(\mathbf{M})\dot{\mathbf{u}}_L \tag{61}$$

The coupling energy that links the two subdomains is given as the following with the contribution of the explicitly computed $\ddot{\mathbf{u}}_\Gamma$, or the equivalent Lagrange multiplier force $\boldsymbol{\lambda}_i$ on both subdomains.

$$W_s^{\mathrm{link}} = \frac{1}{2}(\mathbf{C}_s^{\mathrm{T}}\mathbf{u}_s)\boldsymbol{\lambda}_s; \quad W_L^{\mathrm{link}} = \frac{1}{2}(\mathbf{C}_L^{\mathrm{T}}\mathbf{u}_L)\boldsymbol{\lambda}_L \tag{62}$$

where $\boldsymbol{\lambda}_s$ and $\boldsymbol{\lambda}_L$ are equal an opposite in their contribution. The internal work of Ω_s in Eq. 59 accounts for the energy associated to the filtering zone $\Omega_{\mathcal{F}}$. Isolating this component gives:

$$W_{\mathcal{F}} = \frac{1}{2}\mathbf{u}_{\mathcal{F}}\,\mathrm{diag}(\mathbf{M}_{\mathcal{F}})\,\ddot{\mathbf{u}}_d = \frac{1}{2}\mathbf{u}_{\mathcal{F}}\mathbf{f}_d \tag{63}$$

where overlapping displacements $\mathbf{u}_{\mathcal{F}}$, mass $\mathbf{M}_{\mathcal{F}}$, and with the dissipative force written in terms of $\ddot{\mathbf{u}}_d$ or $\mathbf{f}_d$. As previously derived [45], the total coupled work can be found with the force equilibrium at each Δt_s on interface Γ to give:

$$\mathbf{M}_\Gamma^N\ddot{\mathbf{u}}_\Gamma^N = \mathbf{C}_L^{\mathrm{T}}\boldsymbol{\lambda}_L^N + \mathbf{C}_L^{\mathrm{T}}\mathbf{f}_{\mathrm{int},L}^N + \mathbf{C}_s^{\mathrm{T}}\boldsymbol{\lambda}_s^{n+k} - \mathbf{C}_s^{\mathrm{T}}\mathbf{f}_{\mathrm{int},s}^{n+k} + \delta\mathbf{f}_{\Gamma s}^{n+k} = 0 \tag{64}$$

where the additional force applied at each small step $(\cdot)^{n+k}$ is isolated to Γ, balanced with forces at each large step $(\cdot)^N$ to assume a constant acceleration. In the following section we shall quantify the methods' ability to attenuate spurious waves from the perspective of energy, whilst accounting for the effects of the coupling.

6 Numerical examples

In the following section we present three numerical examples. An investigation into the dissipation of the four aforementioned methods of attenuation is conducted by solving the wave propagation of a 1-D benchmark. A comparison of the reflection properties is made, together with an indication of shortcomings that the Shepard-based projection looks to remedy. The proposed method is then applied to 2-D coupled problems. The propagation of a radially expanding wave and the Taylor impact test are simulated. Monolithic single time step solutions are compared to coupled solutions with the attenuation of spurious reflections.

6.1 Attenuation comparison for 1-D wave propagation

This numerical example looks to continue the investigation into the propagation of monochromatic waves in a 1-D elastic medium. Corresponding to the motivating example presented in Fig. 1, a velocity boundary condition is applied to one end of a long bar in Eq. 1. The simulation is repeated for varying wavelengths of $\lambda \in \{L_s/4, \cdots, L_s/52\}$ resulting in varying frequencies ω of the incident wave. These wavelengths span across the spectrum of compatible and incompatible frequencies in Fig. 4, where the transition between spurious wave reflection to complete transmission is depicted. Once more, the domain is discretised into two consecutive subdomains Ω_s and Ω_L, as summarised in Table 1. Each of these simulations are run with the aforementioned coupling algorithm, leveraging multiple time steps with the asynchronous time integration scheme. The difference in element sizes $h_s = 0.25$ mm and $h_L = 1.0$ mm lead to a time step ratio $m = 4$ between subdomains.

Firstly, an investigation into the conservation of energy for a simulation without attenuation is conducted. In Fig. 9,

Table 1 Geometric, material and temporal properties for each subdomain of the 1D bar for the propagation of monochromatic waves

Subdomain	h [mm]	# of Elem	L [mm]	E [GPa]	ρ [kgmm^{-3}]	Δt (ms)
Small	0.25	500	125	207	7.83×10^{-6}	2.431×10^{-5}
Large	1.00	125	125	207	7.83×10^{-6}	9.724×10^{-5}

The Courant number $Co = 0.5$ is applied to determine the time steps of each subdomain

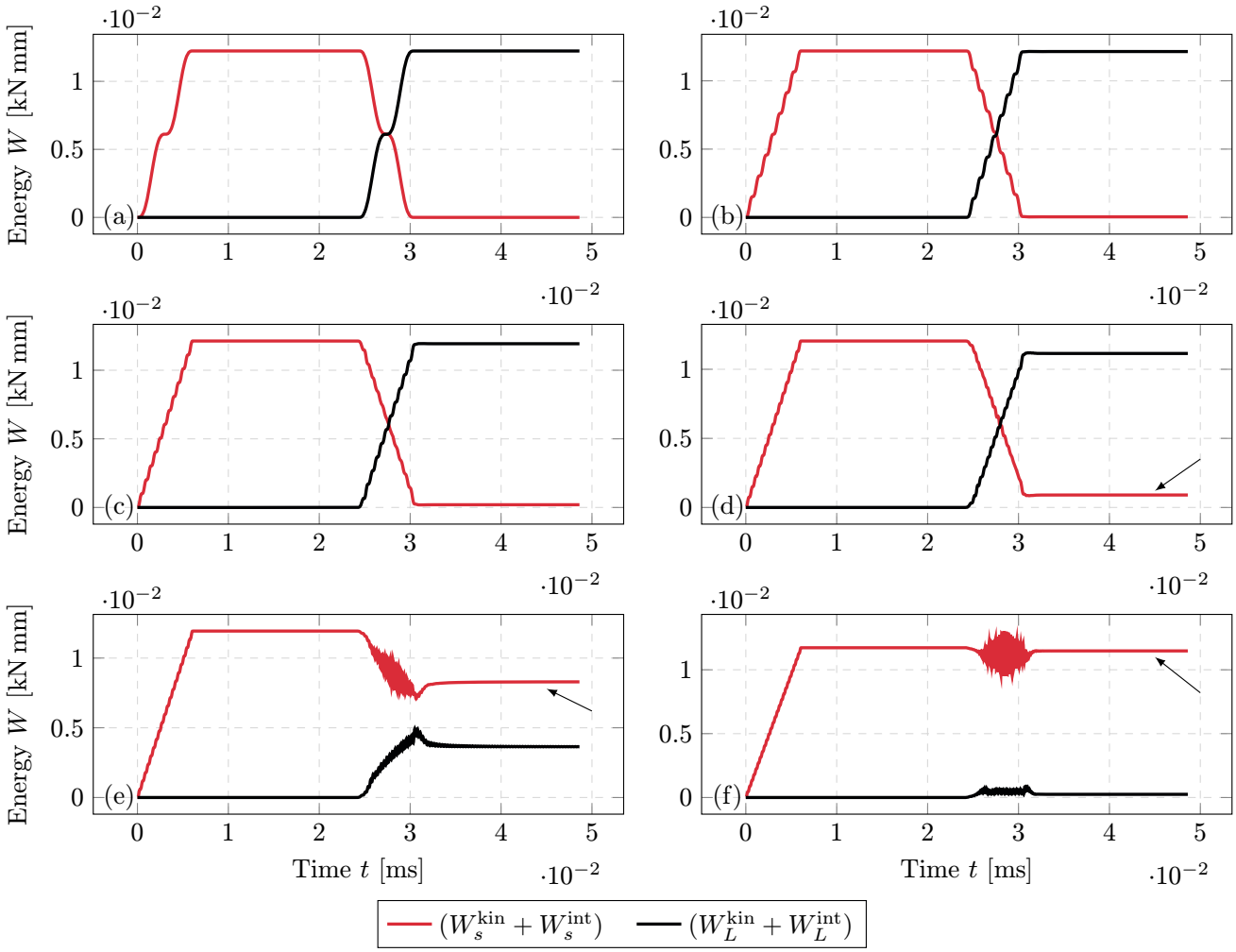

Fig. 9 Total energy of unfiltered simulations for monochromatic frequency study through 1D elastic bar of discretisations $h_s = 0.25$ mm and $h_L = 1.0$ mm integrating with a single time step. The propagating waves are of lengths **a** $\lambda = 31.25$ mm; **b** $\lambda = 7.8125$ mm; **c** $\lambda = 5.2083$ mm; **d** $\lambda = 3.9062$ mm; **e** $\lambda = 3.1250$ mm; **f** $\lambda = 2.4038$ mm

Eqs. 59–62 are utilised to compute the components of energy through time. In this study, we depict the summation of the kinetic and internal components $W^{\text{kin}} + W^{\text{int}}$, where in an elastic simulation, we expect the an entire transfer to these components. Figure 9a depicts the smooth energy transition for a low frequency wave, through to Fig. 9f which depicts a near 100% spurious reflection for a high frequency wave. As highlighted by the red line, the incompatible frequencies result in the energy entrapment of W_s following the wave propagating to the interface Γ at $t = 0.02431$ ms. After $t = 0.03039$ ms, the full incident wave has travelled the length of Ω_s. Following this, an assessment of the energies in Ω_L and Ω_s can be used to quantify the transmission and spurious reflection, respectively. Consequently, a comparison is made between attenuation algorithms through assessing the methods' ability to filter out the incompatible frequencies' energies.

In Figs. 10, 11 and 12, the velocity profiles of the attenuated monochromatic study with multi-time stepping are presented. To compare each of the methods of attenuation,

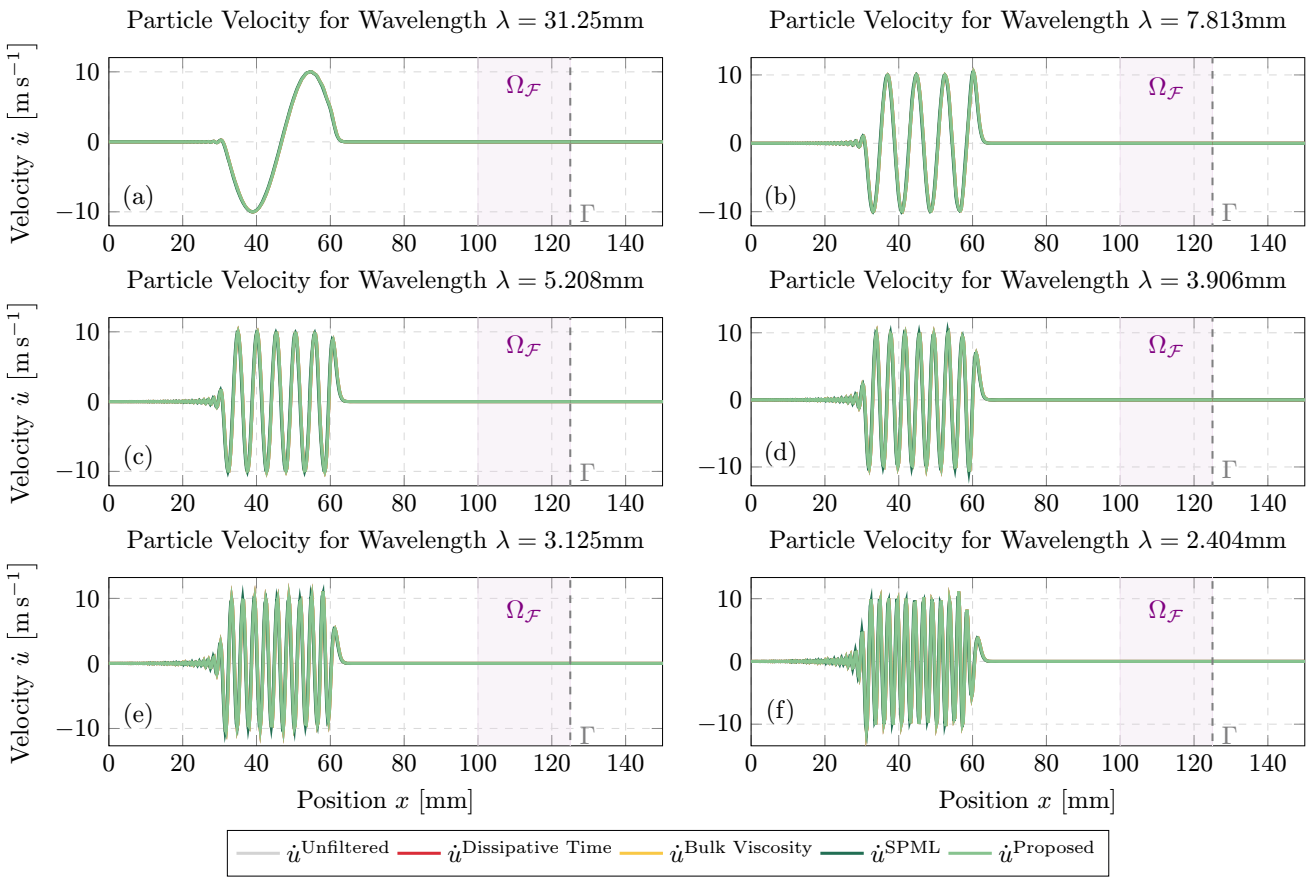

Fig. 10 Velocity distributions after interface Γ interaction at $t = 0.01215$ ms for monochromatic frequency study through 1D elastic bar of discretisations $h_s = 0.25$ mm and $h_L = 1.0$ mm with multi-time stepping

the same length of filtering zone $\Omega_{\mathcal{F}} = \{x \in \mathbb{R} \mid 100 \leq x \leq 125\}$ is used in each simulation. The filter region, depicted in purple, is just a fifth of Ω_s, including the interface Γ between the two subdomains. In the cases of the SPML and Shepard-based projection methods, a constant filtering coefficient of $\gamma_{\mathcal{F}} = 500$ ms^{-1} is utilised for each simulation. IDW parameters utilise the common power $p = 2$ and $k = 2$ for the two nearest neighbours in the distance matrix. Figures 2a–f depict the range of frequencies used, a total of 30 simulations are conducted to compare. At time $t = 0.01216$ ms, the velocity boundary condition has been fully applied to Ω_s. No difference between attenuation methods is visualised at this point in the simulation. At $t = 0.02431$ ms, the incident wave is attenuated by each of the methods in $\Omega_{\mathcal{F}}$. At this stage in the simulation, observations can be made with regards to each method's ability to attenuate. As expected the lower frequency simulations in (a) to (c) are largely unaffected as these frequencies are compatible with both spatial discretisations of Ω_s and Ω_L. Below the cut-off frequency, in (d) to (f), varying levels of dissipation can be observed. Dissipative time integration is seen to be less effective in filtering out the entire spectrum of spurious reflection. However, at this time step, bulk viscosity, SPML and the proposed Shepard-based projection perform similarly. Figure 12a–f depict the velocity fields after the wave travels through $\Omega_{\mathcal{F}}$ at $t = 0.03637$ ms. The dissipative time integration performs poorly in comparison to its counterparts. Visual inspection is not enough to quantify the difference between the other methods. For this we look to quantify the energies in terms of the increments of work.

In Fig. 13 the small subdomain's Ω_s energy through time is highlighted for each simulation. These plots unveil the ability to attenuate of each of the algorithms. The lines in red depict the reflected energy back into Ω_s, with grey the transmitted into Ω_L. To reiterate, granted this is a homogeneous elastic medium, any reflection is purely based on the numerical artifact generated by the mesh. Consequently, we seek the red line to decrease to zero, following the wave fully interacting with $\Omega_{\mathcal{F}}$ at $t = 0.03039$ms. In Fig. 13a, a smooth transmission from Ω_s to Ω_L is visualised. Figures 13b and c show an initial difference between methods, where despite being above the cut-off frequency limit, the transfer of energy is affected. The dissipative time integration method filters significantly less than the SPML and proposed

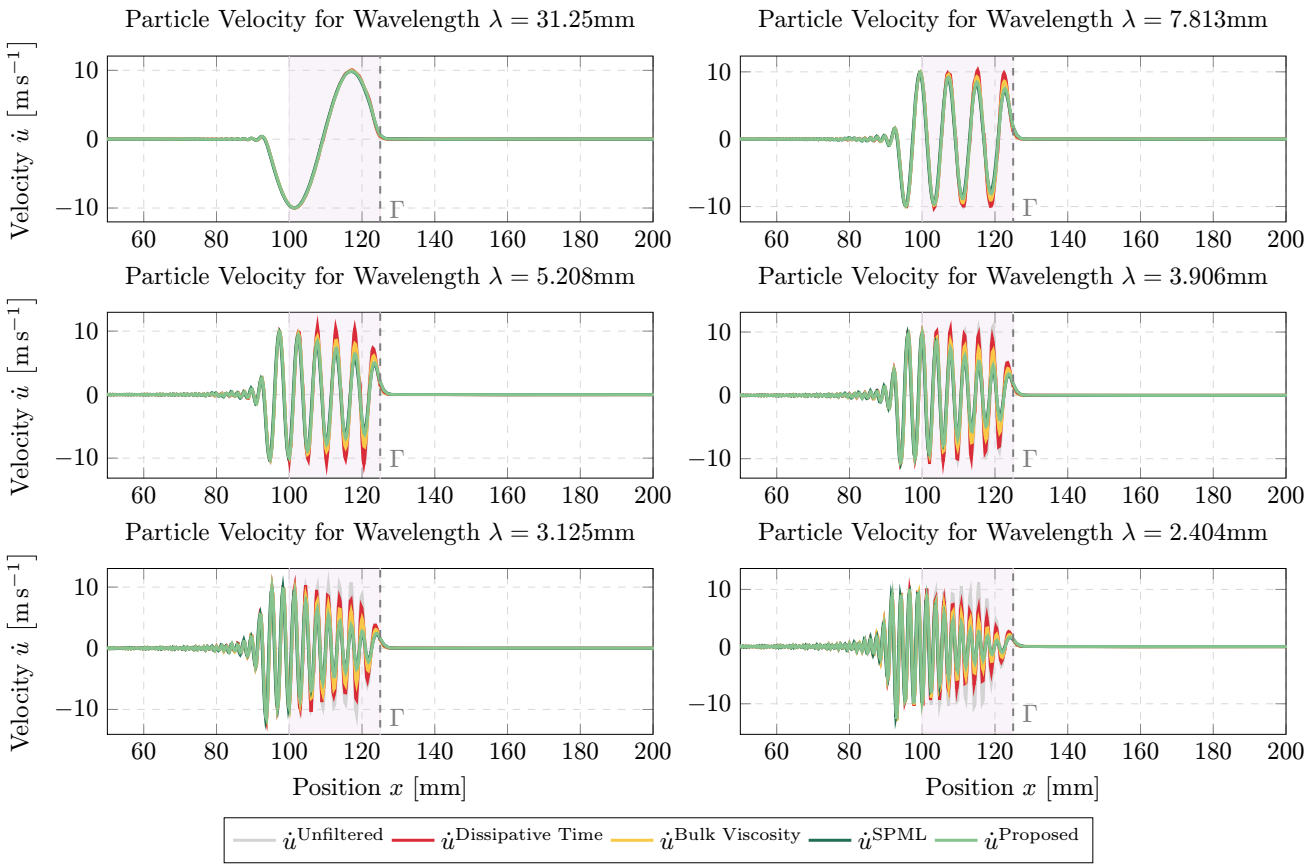

Fig. 11 Velocity distributions after interface Γ interaction at $t = 0.02431$ ms for monochromatic frequency study through 1D elastic bar of discretisations $h_s = 0.25$ mm and $h_L = 1.0$ mm with multi-time stepping

method, with bulk viscosity method in-between. Below the cut-off frequency, spurious reflections are prominent. In this range, the attenuation methods performance contrast vastly. The dissipative time integration method shows the largest amount of reflected energy W_s^{DT} for each of the incompatible frequency simulations. The bulk viscosity method looks to closely match the performance of the SPML and proposed methods, but takes a longer duration of time to have the same effect. The SPML and proposed Shepard-based projection perform well across the range of frequencies.

Evidence of each methods attenuation properties is given through summarising the values of these simulations in Table 2. Above the cut-off frequency, each of the methods perform similarly, with no significant spurious wave reflection expected. However for spurious wave reflections below the cut-off, it is clear that the SPML and the proposed method perform better in attenuating across the wide frequency range of spurious reflections.

In comparison to the aforementioned filtering algorithms, the proposed Shepard-based projection method has proven effective, however the choice of parameters must be mentioned. To do so, we look at varying the parameters in Algorithm 1 with the filtering length $L_{\mathcal{F}}$ and the filtering coefficient $\gamma_{\mathcal{F}}$. The power of $p = 2$ is common for defining the inverse distance weights [42]. For this study, increasing this power proved to be less effective than the filtering length and filtering coefficient. Corresponding to the highest frequency depicted in Figs. 10, 11 and 12, we study the Shepard-based projection method's ability to attenuate an incompatible frequency $\lambda = 2.404$ mm for varying parameters. Considering the attenuation of 99% of the spurious reflection, Marchais et al. stated the reduction of the amplitude in $\Omega_{\mathcal{F}}$ is expressed as an exponential decay of $e^{-\gamma_{\mathcal{F}}\Delta t_{\mathcal{F}}} < 0.01$, where a conservative round trip over a filtering zone requires $\Delta t_{\mathcal{F}} \geq 2L_{\mathcal{F}}/c$ [26]. Consequently, estimation of c with the dilatational wave speed gives the following:

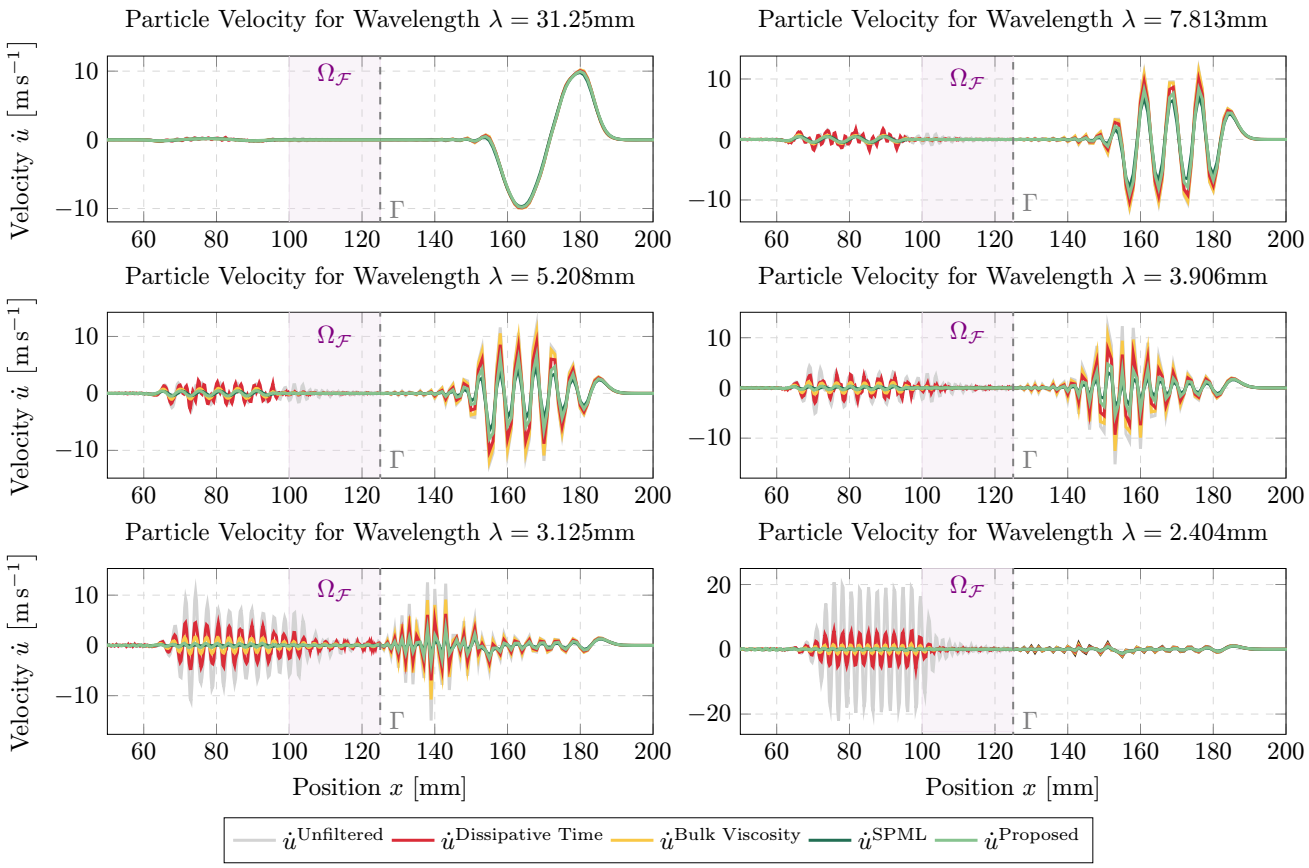

Fig. 12 Velocity distributions after interface Γ interaction at $t = 0.03647$ ms for monochromatic frequency study through 1D elastic bar of discretisations $h_s = 0.25$ mm and $h_L = 1.0$ mm with multi-time stepping

$$\frac{2L_{\mathcal{F}}}{c} > \frac{\ln(100)}{\gamma_{\mathcal{F}}} \approx \frac{4.60517}{\gamma_{\mathcal{F}}} \tag{65}$$

In Fig. 14, the proposed method shows close alignment to the relationship described in Eq. 65, where in Fig. 14a we depict 26 simulations varying the filtering length $L_{\mathcal{F}}$ by increasing the number of overlapping anchor points with a spacing of h_L for a constant filtering coefficient. In Fig. 14b, the filtering coefficient is varied across 21 simulations to show the relationship of increasing the "strength" in the attenuation for a given $L_{\mathcal{F}}$. Both increasing $L_{\mathcal{F}}$ and $\gamma_{\mathcal{F}}$ prove to be effective methods of reducing the spurious reflections, however an appropriate choice of $\gamma_{\mathcal{F}}$ is the more economical option with less IDW weights requiring computation.

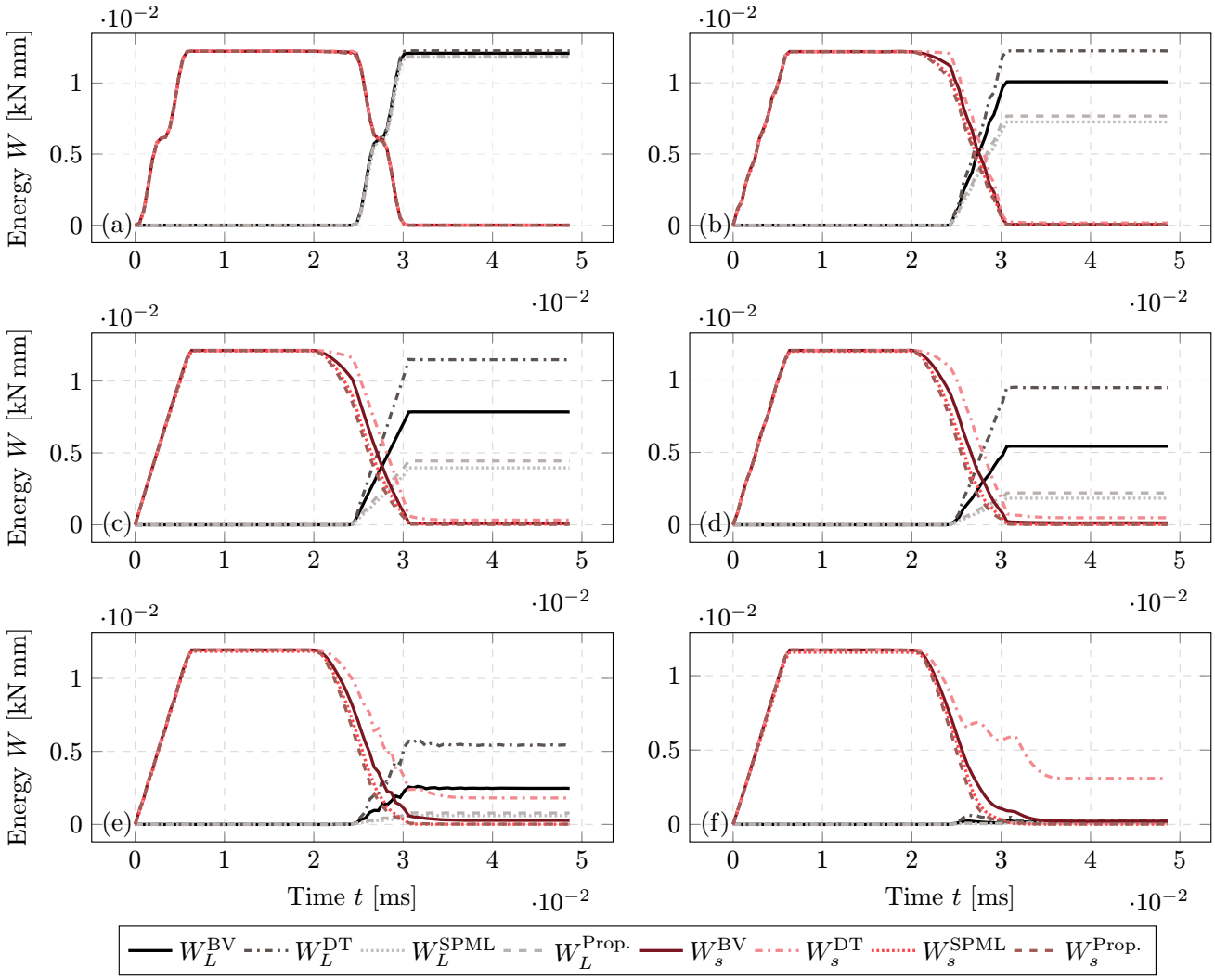

Fig. 13 Comparison of energy dissipated for monochromatic frequency study through 1D elastic bars with multi-time stepping. Each plot depicts the summation of $(W^{\mathrm{kin}} + W^{\mathrm{int}})$ in each subdomain

Table 2 Comparison of methods' ability to dissipate a range of frequencies in the 1-D benchmark. Percentage values represent the energy entrapped in small subdomain Ω_s

	Below Cut-Off Frequency			Above Cut-Off Frequency		
Wavelength [mm]	2.404	3.125	3.906	5.208	7.813	31.25
Bulk Viscosity	1.87%	2.38%	1.10%	0.76%	0.42%	0.03%
Dissipative Time	26.50%	15.37%	4.08%	2.70%	1.33%	0.05%
SPML	0.13%	0.10%	0.23%	0.38%	0.35%	0.03%
Proposed	0.20%	0.18%	0.17%	0.21%	0.21%	0.02%

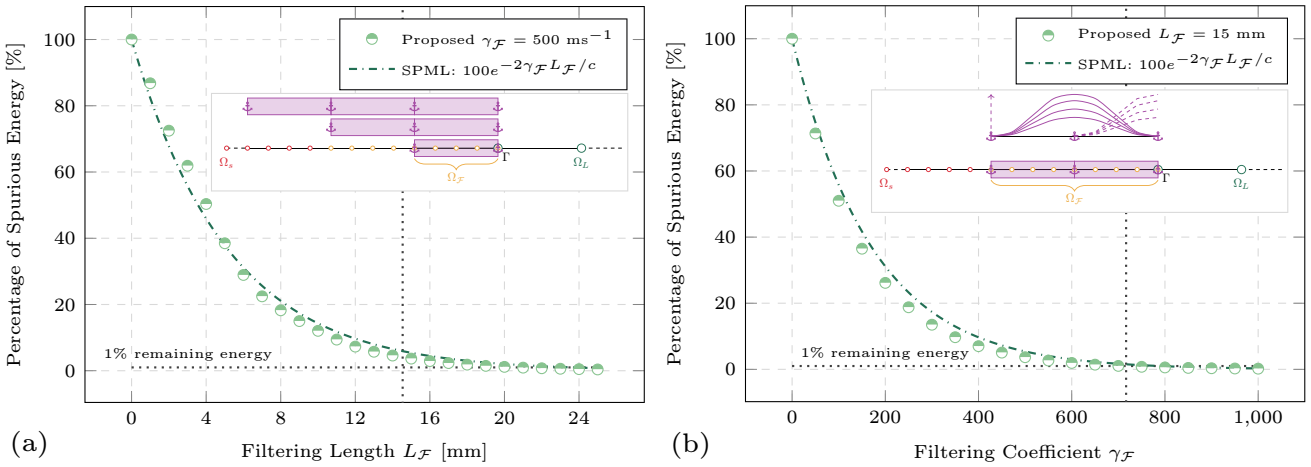

Fig. 14 Shepard-based projection method parameter study with comparison to SPML exponential relationship [26]; **a** varying filtering length $L_{\mathcal{F}}$ for a constant filtering coefficient $\gamma_{\mathcal{F}}$ **b** varying filtering coefficient $\gamma_{\mathcal{F}}$ for a constant $L_{\mathcal{F}}$, where anchor spacing is equivalent to h_L

6.2 Expanding source for 2-D bulk wave propagation

In the following numerical example we demonstrate two aims. Validating the implementation of the method in 2-D, as well as assessing the effectiveness of the proposed algorithm with respect to dissipative parameters.

We consider the radially expanding source, namely the bulk wave propagation problem by Chiappa et al. [58]. The aforementioned works derived a closed form solution for the 2D wave propagation benchmark in an elastic medium. The computational domain is a square of dimensions 1×1 mm^2. Isotropic elasticity is assumed throughout the domain with constants $E = 209$ GPa, $\rho = 7.8 \times 10^{-6}$ kgmm^{-3} and Poisson's ratio $\nu = 1/3$. Those nodes at the centre of the domain $(0.5, 0.5)$, within the area of a 0.1×0.1 mm^2 box are prescribed an initial velocity in the X-direction $\dot{\mathbf{u}}_x = 1\text{ms}^{-1}$:

$$\dot{u}_x(x, y) = 1\text{ms}^{-1} \quad \text{for } (x, y) \in [0.45, 0.55] \times [0.45, 0.55] \tag{66}$$

On the boundary of the domain, a sliding support is given for the outer edges:

$$u_x(0, y) = 0 \quad \text{for } y \in [0, 1]; \quad u_x(1, y) = 0 \quad \text{for } y \in [0, 1] \tag{67}$$

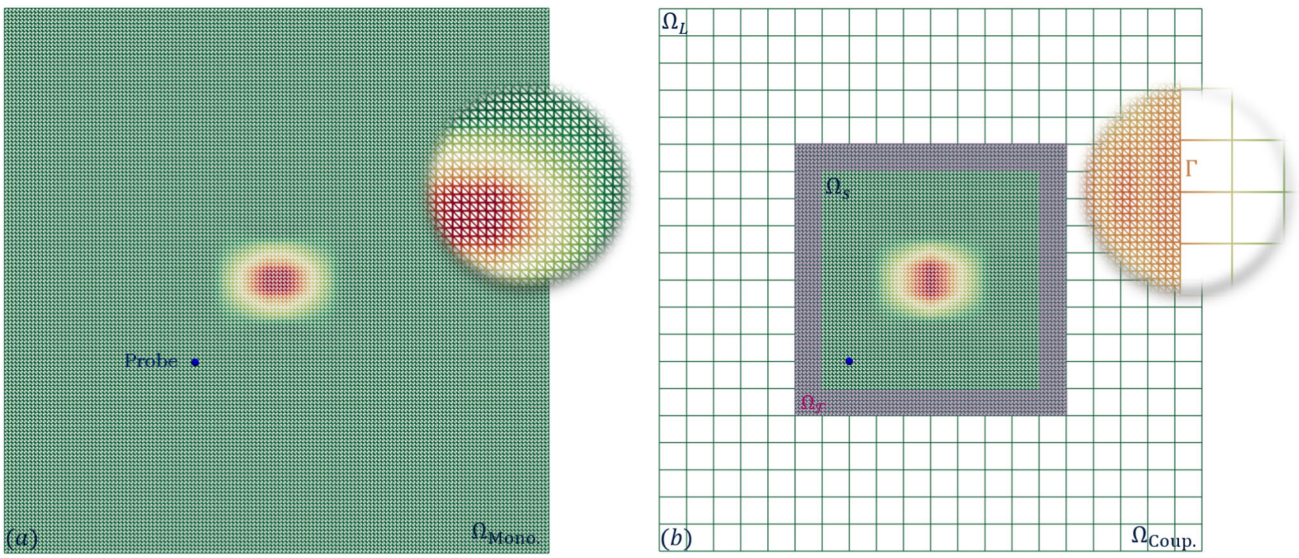

Fig. 15 Expanding wave benchmark; **a** monolithic reference simulation is discretised with a fine mesh matching Chiappa et al. $h_{\text{Mono}} = 0.007$ mm [58] **b** multi-time stepping simulation utilises a mixed discretisation of with $h_s = 0.007$ mm and $h_L = 0.050$ mm with a non-matching interface Γ and filtering zone $\Omega_{\mathcal{F}}$. A probe for displacement evaluations is placed at (0.35, 0.35)

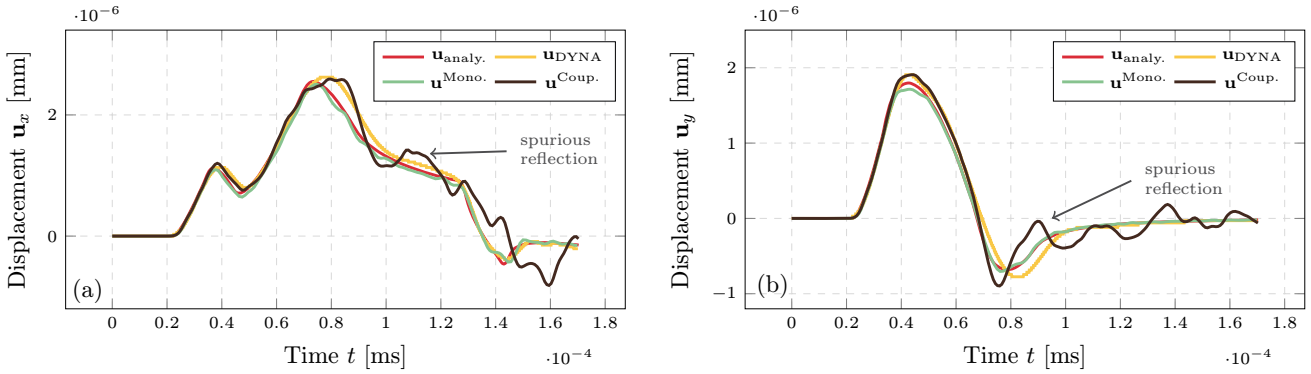

Fig. 16 Comparison between analytical solution derived by Chiappa et al. [58], Ansys LS-Dyna simulation, `ex-fem` Monolithic reference simulation and Coupled solution without attenuation in the fine-coarse mesh; **a** X-Displacement $\mathbf{u}_x$ and **b** Y-Displacement $\mathbf{u}_y$ at probe (0.35,0.35)

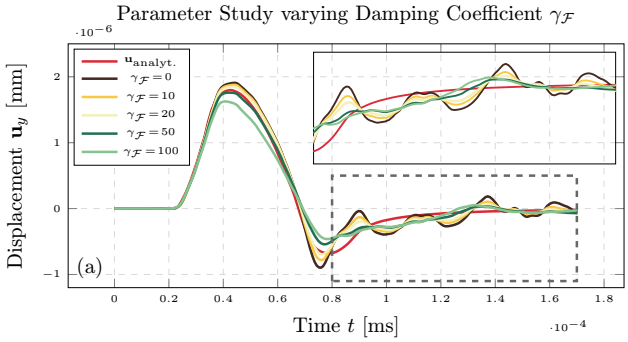

Fig. 17 Displacement profiles of radially expanding wave at (0.35, 0.35); Variation in filtering coefficient for a constant filtering length $L_{\mathcal{F}} = 2h_L$, where values of $\gamma_{\mathcal{F}}$ are given in ms^{-1}

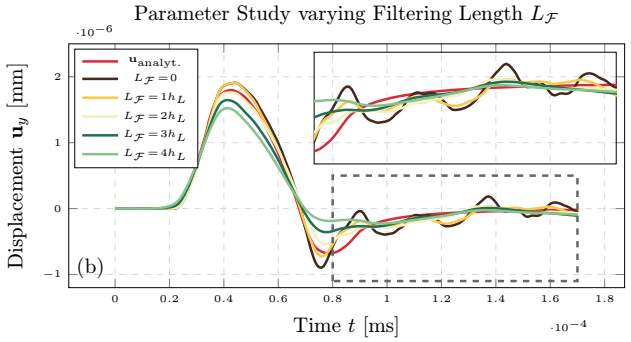

Fig. 18 Displacement profiles of radially expanding wave at (0.35, 0.35); Variation in filtering length $L_{\mathcal{F}}$ where thickness of the zone is determined by the large element size h_L

$$u_y(x, 0) = 0 \quad \text{for } x \in [0, 1]; \quad u_y(x, 1) = 0 \quad \text{for } x \in [0, 1] \tag{68}$$

These conditions result in an expanding wave, that reflects back into the centre, once the wave reaches the boundary of the domain. Simulations are performed in an in-house finite element code `ex-fem`, where the comparison of traditional explicit FEM methods to coupled methods with attenuation can be made.

We compare two spatial discretisations; a monolithic reference simulation with a single time step, followed by a coupled solution with a non-matching fine-coarse mesh and multi-time stepping with small-large time steps. Figure 15a and b illustrate the two spatial discretisations, as well as the contours of the initially applied velocity. In the case of the monolithic simulation, the domain $\Omega = [0, 1] \times [0, 1] \subset \mathbb{R}^2$ is discretised to match the element size of Chiappa et al. of $h_{\text{Mono.}} = 0.007$ mm, with linear triangular elements, to give a total of 40,898 elements and 20,736 nodes.

In the case of the coupled domain the same physical problem is solved, but with a heterogeneous discretisation in both space and time. Let the partitioning of domain Ω be written as:

$$\Omega = \Omega_s \cup \Omega_L; \quad \Omega_s = [0.25,\ 0.75] \times [0.25,\ 0.75]; \quad \Omega_L = [0,\ 1] \times [0,\ 1] \setminus \Omega_s \tag{69}$$

with interface $\Gamma = \{(x, y) \in [0.25, 0.75]^2 : x \in \{0.25, 0.75\} \text{ or } y \in \{0.25, 0.75\}\}$. A mixed discretisation of triangular elements with $h_s = 0.007$ mm and quadrilateral elements $h_L = 0.05$ mm is utilised to give an abrupt step in mesh resolution. The small subdomain Ω_s is discretised with a total of 10,368 elements and 5,329 nodes, with Ω_L comprising of just 300 elements and 360 nodes. Following the guidance of Chiappa et al., where the analytical solution of the problem is derived, the frequency spectrum can be determined without the truncation found in the Fourier transform [58]. The choice of mesh size $h_{\text{Mono.}}$ and h_s allows for 99% of the frequency band to be captured. This is unlike h_L, which is even larger than the less conservative Nyquist-Shannon sampling rate that would require $h_{N-S} = 0.02438$ mm. From this, it is clear spurious reflections will be generated with the inability of Ω_L to capture higher frequencies. An additional coupling simulation is compared with the addition of a fil-

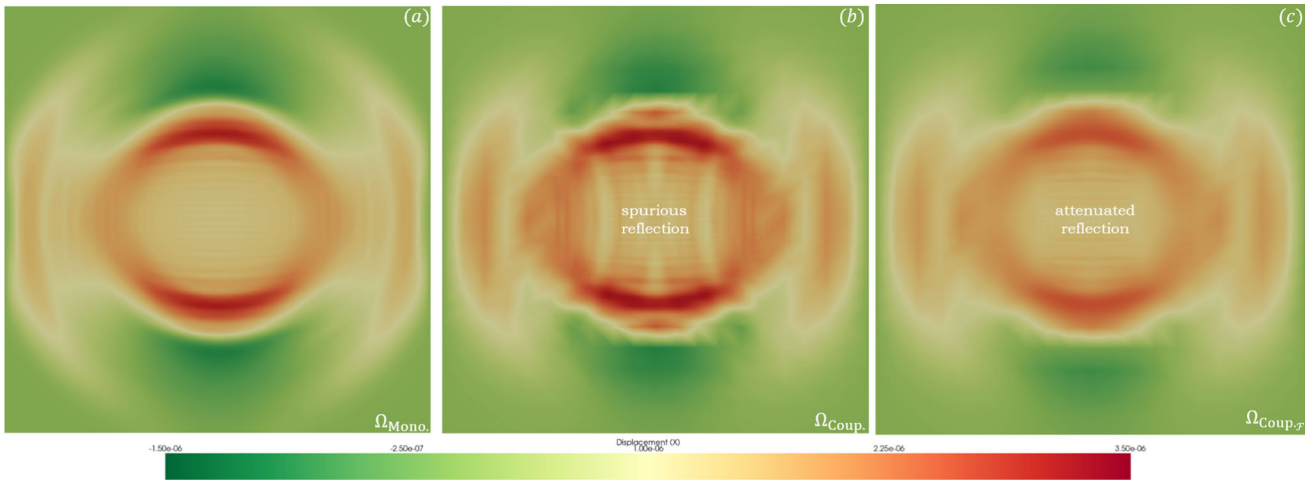

Fig. 19 X-Displacement at $t = 7.82$ ms for expanding source; **a** monolithic reference mesh using triangular elements of $h_{\text{Mono}} = 0.007$ mm; **b** Coupled simulation with a mixed discretisation of triangular $h_s = 0.007$ mm and quadrilateral $h_L = 0.050$ elements depicts reflections with disparate mesh sizes and multiple time steps; **c** Attenuated waves with use of the Shepard-based projection

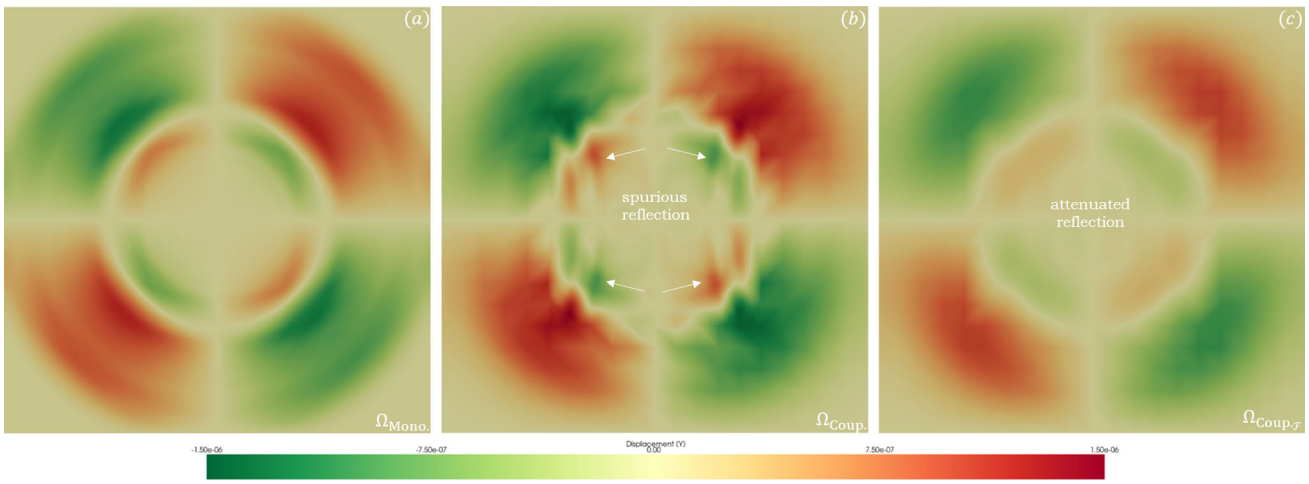

Fig. 20 Y-Displacement at $t = 7.82$ ms for expanding source; **a** Monolithic reference mesh using triangular elements of $h_{\text{Mono}} = 0.007$ mm; **b** Coupled simulation with a mixed discretisation of triangular $h_s = 0.007$ mm and quadrilateral $h_L = 0.050$ elements depicts reflections with disparate mesh sizes and multiple time steps; **c** attenuated waves with use of the Shepard-based projection

tering zone described by an overlapping portion of Ω_s close to the interface as defined by:

$$\Omega_{\mathcal{F}} = \{(x, y) \in [0.25, 0.75]^2 : \min(x - 0.25,\ 0.75 - x,\ y - 0.25,\ 0.75 - y) \leq L_{\mathcal{F}}\} \quad (70)$$

where we denote $\Omega_{\mathcal{F}}$ contained within the small subdomain, and $L_{\mathcal{F}}$ as the filtering length for attenuation. Each of the simulations are run for a total time $t = 1.7 \times 10^{-4}$ ms with $Co_{\text{Mono.}} = Co_s = Co_L = 0.1$. The difference in discretisations lead to a non-integer time step ratio of $m = 7.2$ between large and time step in the coupled simulation. We denote $\Omega_{\text{Mono.}}$ and $\Omega_{\text{Coup.}}$ as the monolithic reference domain and coupled domain with multi-time stepping, respectively.

To validate the implementation in `ex-fem`, we first simulate the monolithic reference simulation of Fig. 15a. Figure 16a and b compares the X and Y displacement, at a probe positioned $(0.35, 0.35)$, to the closed form analytical solution, as well as analysing the problem in commercial software Ansys LS-DYNA. The monolithic simulation shows very close agreement to the analytical solution, even of higher accuracy than its commercial counterpart. Figure 16a and b also depicts the issue of the coupled solution with the disparate mesh sizes. It is clear that the solution cannot match the accuracy of the monolithic solutions, however it also shows

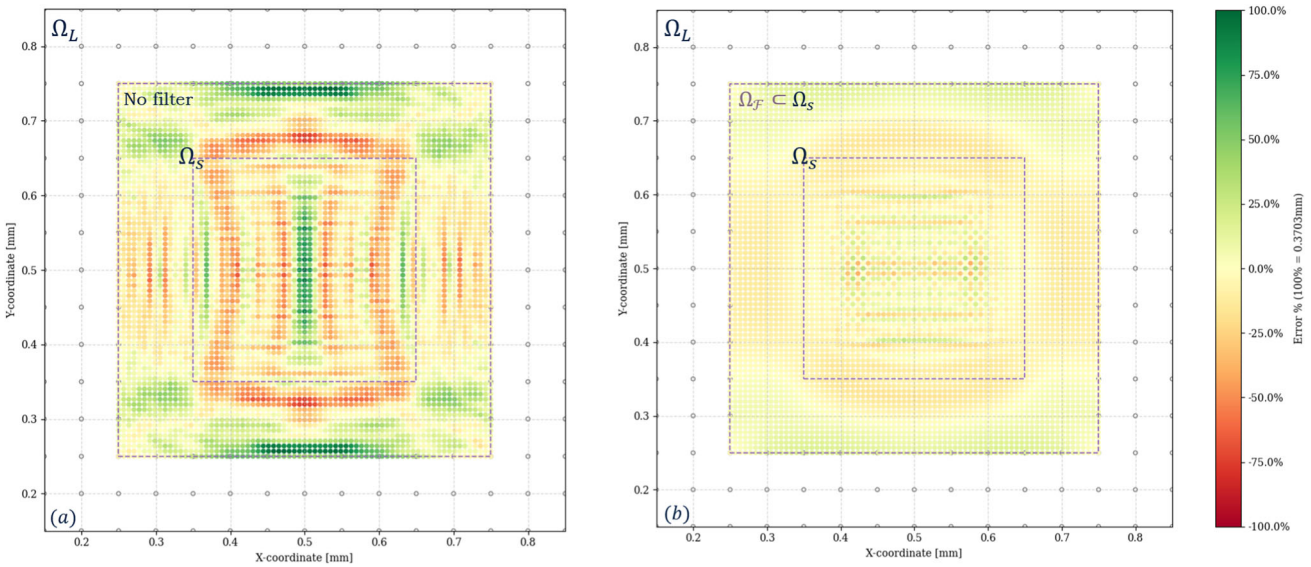

Fig. 21 X-Displacement error at $t = 7.82$ ms for expanding source benchmark with initial velocity $\dot{\mathbf{u}}_x = 1\text{ms}^{-1}$ compares Ω_{Mono} with small subdomains of **a** unfiltered coupled solution $\Omega_{\text{Coup.}}$ depicts spurious waves; **b** filtered coupled solution $\Omega_{\text{Coup.}_\mathcal{F}}$ shows attenuation of waves

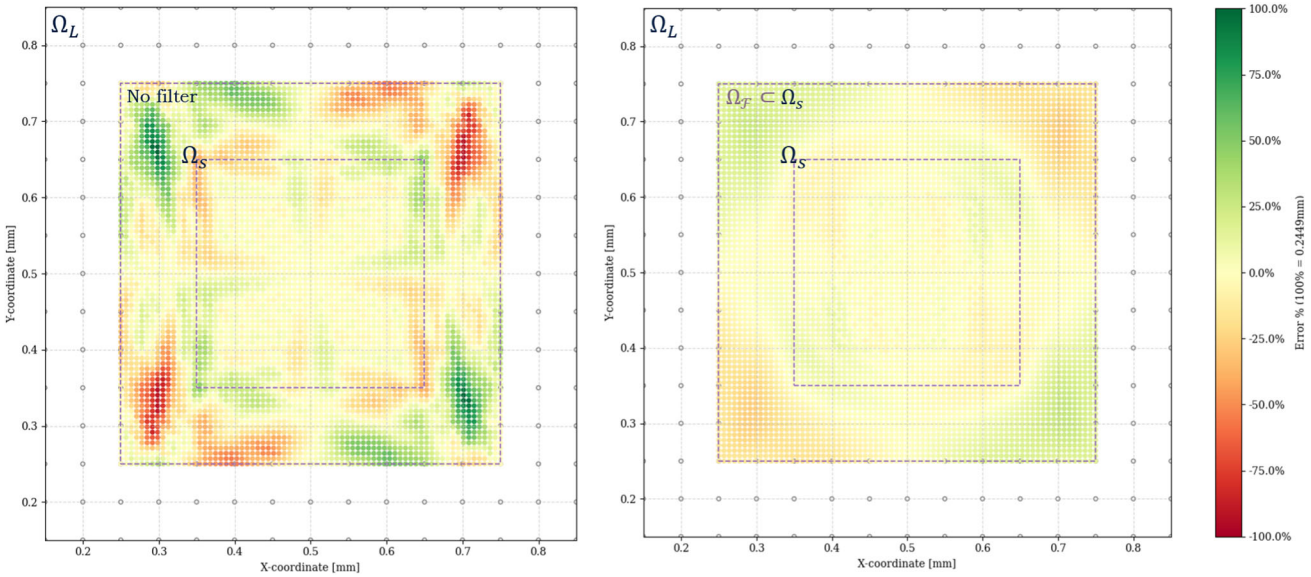

Fig. 22 Y-Displacement error at $t = 7.82$ ms for expanding source benchmark with initial velocity $\dot{\mathbf{u}}_x = 1\text{ms}^{-1}$ compares Ω_{Mono} with small subdomains of **a** unfiltered coupled solution $\Omega_{\text{Coup.}}$ depicts spurious waves; **b** filtered coupled solution $\Omega_{\text{Coup.}_\mathcal{F}}$ shows attenuation of waves

spurious artifacts that follow the interaction of the wave at the interface Γ between the two meshes. Through implementing the Shepard-based projection, we look to improve the solution of the coupled domain with $\Omega_\mathcal{F}$ attenuating these spurious oscillations.

Subsequently, we look to assess the effect of these key parameters on the attenuation of the spurious waves. Using the displacement probe $\mathbf{u}_y$ as reference, a parametric study looks to vary first the filtering coefficient $\gamma_\mathcal{F}$, and then the filtering length $L_\mathcal{F}$. Under the assumption of a constant $L_\mathcal{F} = 2h_L$ coupling length, Fig. 17a depicts the effect of increasing $\gamma_\mathcal{F}$. The results show an increasing amount of attenuation as $\gamma_\mathcal{F}$ increases. Figure 18 shows increasing the filtering length $L_\mathcal{F}$ for a given filtering coefficient of $\gamma_\mathcal{F} = 50\ \text{ms}^{-1}$ also increases attenuation. However, unlike varying $\gamma_\mathcal{F}$, increasing $L_\mathcal{F}$ comes with an additional computational cost of computing more inverse distance weights $\mathbf{w}$ and applying the projection over more nodes in $\Omega_\mathcal{F}$. Both depict the importance of parameter selection, ensuring the attenuation of the incompatible frequencies, but also not over-dampening the solution with too large a filtering length

Table 3 Comparison of computational runtimes for expanding wave propagation benchmark. The coupled algorithm utilises attenuation parameters $\gamma_{\mathcal{F}} = 100\ \text{ms}^{-1}$ and $L_{\mathcal{F}} = 3h_L$

Monolithic reference	Coupled with MTS	Coupled with MTS and Proposed filter
1301.8 s	354.6 s	379.0 s

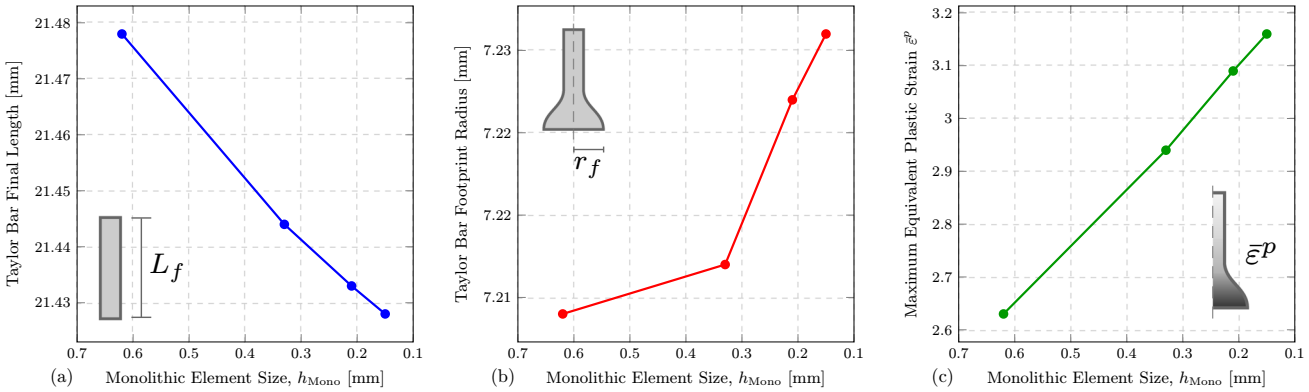

Fig. 23 Convergence study for monolithic simulations of the Taylor Bar Impact for varying mesh sizes h_{Mono} discretising the bar with 5×50, 10×100, 15×150 and 20×200 elements. The metrics used to evaluate convergence include; **a** final length of Taylor Bar, **b** footprint radius of Taylor Bar and **c** maximum equivalent plastic strain

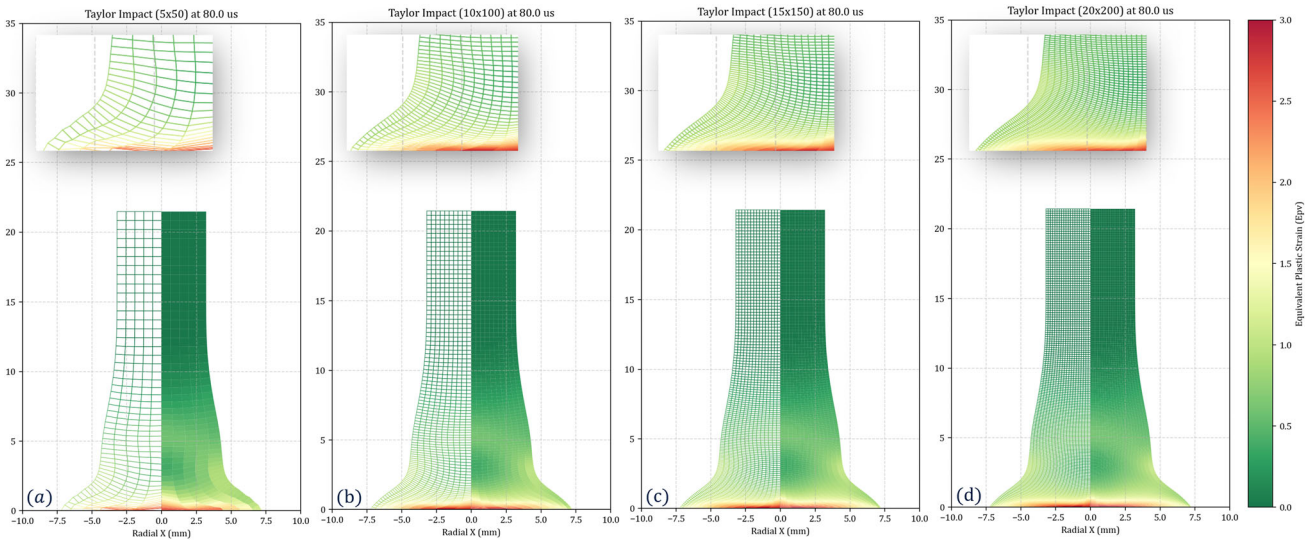

Fig. 24 Monolithic reference simulations of the Taylor bar impact with equivalent plastic strain $\bar{\varepsilon}^p$ plotted with increasing mesh resolutions; **a** 5×50; **b** 10×100; **c** 15×150; **d** 20×200 Elements

$L_{\mathcal{F}}$ or filtering coefficient of $\gamma_{\mathcal{F}}$. For this simulation we find $L_{\mathcal{F}} = 3h_L$ and $\gamma_{\mathcal{F}} = 100\ \text{ms}^{-1}$ to be effective.

In Fig. 19, we depict the displacements in the X-direction at $t = 7.82$ ms. Whilst the monolithic reference simulation in Fig. 19a aligns well with the works of Chiappa et al., the coupled solution in Fig. 19b with non-uniform meshes leads to a strong reflection back into Ω_s. These spurious reflected are targeted for attenuation with use of the Shepard-projection method in Fig. 19c. Similar observations can be made, assessing the expanding wave in the Y-direction at the same point in time. The monolithic reference of Fig. 20a shows the expanding wave radially, whereas the coupled solution in (b) with the small-large mesh produces artifacts that lead to spurious artifacts. These spurious oscillations are suppressed in Fig. 20c, but a slight difference can still be visualised between the coupled and reference simulation. This highlights the Shepard-based projection method's ability to dissipate spurious modes, however it cannot improve the solution in Ω_L, where spatial resolution cannot capture the full spectrum of

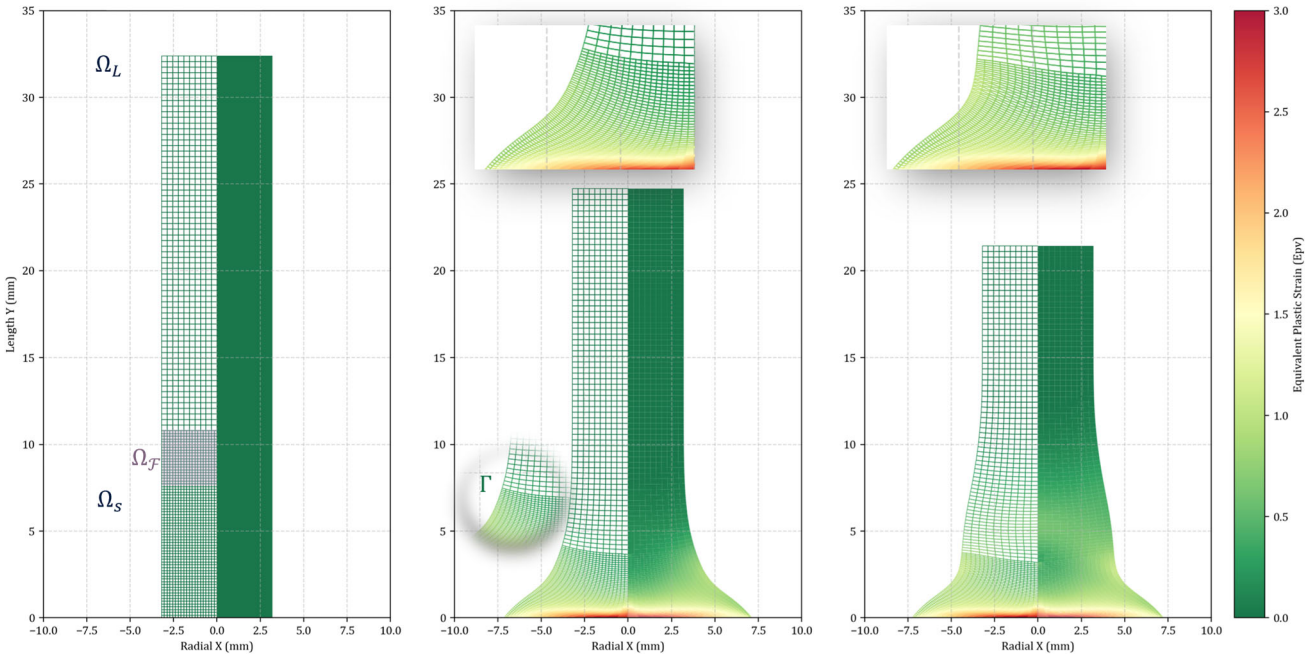

Fig. 25 Coupled simulations of the Taylor Bar Impact for varying mesh sizes integrated over multiple time steps. A filtering zone $\Omega_{\mathcal{F}}$ is defined within Ω_s where 10×10 overlapping points are defined. The deformation of the bar is captured at time steps, **a** 0.0μs, **b** 38.92μs **c** 80.0μs

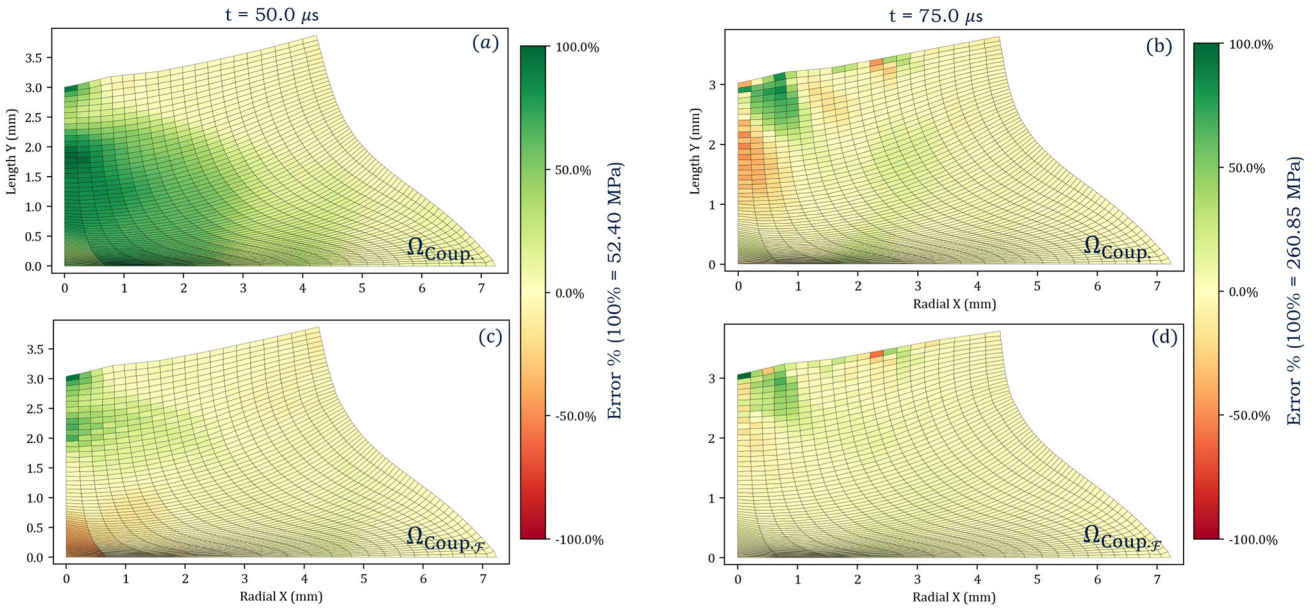

Fig. 26 Effective stress error at for the Coupled Taylor impact test compares Ω_{Mono} with small subdomains of at times $t = 50.0\mu$s and $t = 75.0\mu$s for **a** unfiltered coupled solution $\Omega_{\text{Coup.}}$; **b** filtered coupled solution $\Omega_{\text{Coup.}}$; **c** unfiltered coupled solution $\Omega_{\text{Coup.}}$; **d** filtered coupled solution $\Omega_{\text{Coup.}_{\mathcal{F}}}$; where all coupled subdomain use multi-time stepping

Table 4 Comparison of Taylor Bar Impact metrics at final time $t = 80.0\mu$s

Simulation	Final Length	Footprint Radius	Maximum Equivalent Plastic Strain
Monolithic (20×200)	21.43	7.23	3.16
Coupled (10×67 and 20×67)	21.43	7.24	3.15
Pantalé DynELA [59]	21.42	7.17	3.26

Table 5 Comparison of Computational runtimes for Taylor Bar Impact. The coupled algorithm utilises attenuation parameters $\gamma_{\mathcal{F}} = 100$ ms^{-1} and $L_{\mathcal{F}} = 10h_L$

Monolithic Reference	Coupled with MTS	Coupled with MTS and Proposed Filter
19,104.9 s	7,018.7 s	8,888.0 s

frequencies. Rather, the propagation of low frequency waves are observed under the limitation of the local element size.

Evaluations of error are made for this simulation in Figs. 21 and 22 to compare displacement contours of the coupled solutions to the monolithic reference solution. We assess the Shepard-based projection's ability to filter by quantifying the error in Ω_s, where the method adopted reduces the spurious waves in both dimensions. The displacement errors are normalised with the maximum values of error for their respective dimensions. A severe reduction in spurious reflections are observed, therefore maintaining better accuracy in the fine region. This enables the coupling of disparate spatial and temporal resolutions, whilst alleviating the concerns of the incompatible frequencies distorting the solution significantly.

The computational runtime of each of the simulations is summarised in Table 3. Through invoking the partitioning of the domain with fine and coarse meshes, as well as integrating with multiple time steps a speedup of 3.67× is achieved with the coupled simulation. However, this simulation contains the polluted solution with the spurious wave reflection. We correct this with the comparison of the filtered coupled simulation. The filtering requires further computational effort, however still achieves a significant speedup of 3.43×.

6.3 Taylor bar impact test

In previous sections, we demonstrate the proposed method's capability with simple configurations that simulate linear elasticity. In this example we look to extend its application through applying the coupling with attenuation in elasto-plastic materials. We simulate the Taylor impact test for an OFHC copper specimen, as found in the works of Pantalé [59]. The geometry is a cylindrical copper rod, described with an initial radius $r_0 = 3.2$ mm and length $L_0 = 32.4$ mm, subjected to an impact velocity of 227 ms^{-1}. To reduce computational cost, a half-axisymmetric domain is simulated with the axis of symmetry at $x = 0$ mm. The OFHC copper is modelled with a J2 elasto-plastic constitutive model, invoking linear isotropic hardening. A standard objective stress update with a radial-return correction is implemented in `ex-fem`. The material properties include a Young's modulus $E = 117$ GPa, density $\rho = 8.93 \times 10^{-6}$ kg mm^{-3}, Poisson's ratio $\nu = 0.35$ and yield stress $\sigma_y = 400$ MPa. A linear hardening modulus of $H = 100$ MPa is used, such that the yield stress evolves according to $\sigma_y(\epsilon^p) = 400 + 100\epsilon^p$ MPa. Boundary conditions are applied with nodal coordinates $y > 0$ assigned the initial axial velocity 227 ms^{-1}, with those nodes at $y = 0$ constrained to have zero axial velocity, representing a frictionless rigid wall. The initial excitation results in a sharp compressive stress wave containing a broad range of frequencies, where the loading is close to a step-like impact condition. Nodes on the symmetry axis $x = 0$ are constrained with $\dot{\mathbf{u}}_x = 0$. The problem is run in the case of both monolithic and multi-time step solutions to a final time of 80.0 μs.

We initially assess the performance of a monolithic simulation, conducting a mesh sensitivity analysis of the problem with a single time step. Four meshes of increasing refinement are studied with a quadrilateral mesh, defined by the number of elements in X and Y that define a structured mesh in the bar. Figures 24a–d depict the progressive increase in element count, simulating 5×50, 10×100, 15×150, and 20×200 elements in each direction, respectively. In each plot, we illustrate the final deformed mesh on the left and the equivalent plastic strain contour on the right. Visually, the monolithic meshes perform similarly, however an indication of significant hourglassing can be seen in the coarsest variation. We quantify the performance of the Taylor bar with the common metrics of final length L_f, footprint radius r_f and maximum equivalent plastic strain $\bar{\varepsilon}^p_{\max}$. Figure 23 plots the convergence of each of these metrics as the mesh is refined. The final bar length decreases monotonically towards 21.43 mm, while the footprint radius increases up to 7.23 mm. The maximum equivalent plastic strain is more mesh sensitive, rising from 2.63 to 3.16.

The coupled variation maintains the same Taylor impact physics as the monolithic simulations, the key difference being the single monolithic domain is replaced by two non-matching subdomains coupled with coordinates along a third of the bar length at $Y = 10.8$ mm. The coupled simulation runs the multi-time stepping algorithm, allowing the upper two thirds of the mesh in Ω_L to run on double the time step of Ω_s. We elect to couple mesh sizes with the discretisation of Ω_L using 10×67 quadrilateral elements and Ω_s with 20×67 elements. A 10×10 coarse overlay of anchor points is used below the interface Γ, with a filtering coefficient $\gamma = 100$ ms^{-1} (see Fig. 25).

In Fig. 26, we plot the error in the effective stress output, comparing the finest monolithic single time step solution with the coupled solutions with and without the Shepard-based projection method to filter. As per the previous example, the

error is normalised with the maximum value for the fine subdomain. At times 50.0μs and 75.0μs, Fig. 26a and b depict the effect of the spurious oscillations, caused by the mismatch in subdomain mesh sizes. This error is significantly reduced in Fig. 26c and d with the Shepard-based projection method. The remaining error seen after applying the filter is observed to be in regions of the bar with low effective stress.

The final metrics for each of the simulations is tabulated in Table 4, where strong agreement between the monolithic, coupled and the aforementioned works of Pantalé [59]. Despite, spurious waves being generated at the interface of the non-uniform meshes, their contribution to the final metrics looks to be insignificant. This highlights the algorithm's ability to target the non-physical high-frequency oscillations, rather than the dominant low-frequency momentum transfer that controls the mushrooming response. Plastic dissipation may also render the final deformation less sensitive to high-frequency oscillations reflected from the interface. Specifically, plastic flow and the strain hardening act to dampen the propagation of these waves, thereby limiting their transmission to the impacted lower end. These results suggest that plasticity may facilitate the attenuation of spurious reflections, indicating that the proposed filter is likely less critical in the plastic regime than in its purely elastic counterpart.

The use of a spatial refinement factor and time step ratio $m = 2$ leads to a significant decrease in runtime for the coupled simulations, as tabulated in Table 5. The additional computational cost of the Shepard-based projection method is evident, however a speedup, in comparison to the monolithic reference simulation, can still be observed. The Taylor impact test highlights the method's ability to keep the high-deformation impact zone, whilst replacing the upper more slowly deforming part of the rod with a coarser mesh and multi-time stepping, without excessive numerical pollution from the interface.

7 Conclusion

A new method for the attenuation of spurious wave reflection has been proposed. The issue of spurious reflections occur when spatial discretisations are unable to capture waves of incompatible frequencies from fine to coarse discretisation. In this work, we have developed a Shepard-based projection method that targets these incompatible frequencies, thus preventing spurious wave reflection. The method builds upon the SPML and the weak staggered coupling, by proposing an alternative basis that invokes an inverse-distance weighting [17, 26]. Rather than constructing a fixed mesh with Lagrangian shape functions, distances between the underlying fine discretisation and a set of overlapping coarse anchor points, provide a simple means of projection. Whilst the attenuation can be utilised in uncoupled problems, the benefits of its use is further pronounced in a dynamically coupled setting. Multi-time step integration with non-matching meshes enable this coupling [45]. Together this creates a framework for increasing computational efficiency, whilst filtering out spurious reflections. The method employs an equivalent Lagrange multiplier force within each subdomain, with the interfaces' dynamics being explicitly resolved through the application of a coarse restriction operator.

Comparison between the proposed method to SPML and other common methods of attenuation; including bulk viscosity and a dissipative time integration scheme has been conducted. Testing across a spectrum of frequencies, the analysis in 1-D quantified the amount of spurious energy reflected in a coupled bar of disparate spatial discretisations. Each filtering method integrated utilising asynchronous schemes, where coarse and fine discretisations were permitted to use large and small time steps. Among the key findings, it has been established that the proposed method was able to dissipate 99% of the spurious reflections' energy below the cut-off frequency of the mesh. This improved upon the likes of bulk viscosity and dissipative time integration across a wide range of frequencies, whilst reaching similar levels of accuracy to SPML, with an alternative and simpler projection. The results presented show the effects of filtering parameters on the level of dissipation, confirming the exponential decay relationship. Increasing the filtering coefficient $\gamma_{\mathcal{F}}$ and filtering length $L_{\mathcal{F}}$ effectively reduce spurious reflections, however their values should not be so large to increase impedance mismatch and computational cost, respectively. The study of filtering spurious reflections in 2-D was examined with use of an expanding wave and the Taylor impact test. Through harnessing multiple time steps and relaxing the mesh constraints with non-matching interfaces, a clear speedup in computation is achieved.

This paper highlights the potential of a Shepard-based projection method to serve as a spurious wave reflection filter, enabling a more accurate spatial and temporal coupling for explicit finite element subdomains. However, further research is required in the exploration of the filtering domain's geometry. Further work also includes employing the coupling with attenuation in settings where mesh ratios between coarse and fine subdomains vastly exceed those demonstrated in this paper. Whilst, the extension to 3-D should be trivial, efforts to more complex models with enclosed curved areas or volumes of $\Omega_{\mathcal{F}}$ should also be made. The method could also be proposed for usage in adaptive or crack propagation settings, where not only explicit finite elements can be used, but also other meshless approaches [60, 61]. Finally, attenuation methods that are conservative, rather than dissipative could also be of interest, combining with methods that explore other kernel approximations to tackle spurious oscillations in wave propagation applications [62–

64]. These developments support the motivation for topics of research to come.

Appendix A Other benchmarks for appendix

A. 1 Superposition of frequencies for 1D propagation

An additional benchmark is conducted with a similar setup to the problem described in Sect. 6.1 to demonstrate the performance of the proposed attenuation strategy in comparison to those methods mentioned in literature. The computational domain consists of two subdomains; a fine discretisation (small elements) and coarse discretisation (large elements). The problem is representative of scenarios where local refinement is required in regions of interest, whilst coarser representations are used elsewhere to reduce computational cost. The problem consists of two consecutive subdomains of equal length $L_s = L_L = 125$ mm, where both are modelled as elastic bars with identical material properties. Representing a steel-like behaviour material properties are $E = 207$ GPa, density 7.83×10^{-6} kg/mm^3 and cross-sectional area $A = 1.0$ mm^2. The dilatational wave speed in each element $c_e = 5141$ mm/ms gives a total wave travel time of $t_{\text{final}} = 0.04862$ ms which is used as the total simulation time. The subdomains are spatially discretised with linear elements of size $h_s = 0.25$ mm and $h_L = 1.0$ mm to give a total of 500 small elements and 125 large elements. This results in a refinement factor of four between Ω_s and Ω_L. Time integration is employed with the leapfrog scheme with a CFL number $Co_s = Co_L = 0.5$ in each subdomain. The mesh disparity allows for a temporal discretisation such that four fine-scale time steps Δt_s equal one coarse time step Δt_L. To account for this, the aforementioned multi-time stepping scheme is incorporated [45].

Excitation to Ω_s is defined as the superposition of two harmonic components with distinct wavelengths:

$$\dot{u}(t) = 10.0 \sin(2\pi\omega_{lf} t) + 1.0 \sin(2\pi\omega_{hf} t) \tag{A1}$$

where low frequency and high frequency components correspond to:

$$\lambda_{lf} = L_s/4; \quad \lambda_{hf} = L_s/68; \tag{A2}$$

to yield two simulations, where we look to see the effects with and without attenuation.

In Fig. 27, the 1-D simulation is presented without spurious wave attenuation. The incident wave can be plotted in (a), after the wave has travelled half of Ω_s, to observe the superimposed frequencies. This scenario leads to the higher frequency being reflected upon interacting with the interface. In Fig. 27b, the transmission of the ω_{lf} reaches half of Ω_L, whereas ω_{hf} is fully reflected. This indicates the presence of spurious wave oscillations due to the mismatch in spatial discretisation. Note similar results are acquired, regardless of single time step or multi-time step solutions. Next, we look to filter these spurious oscillations through re-implementing methods of literature and the proposed Shepard-based projection method.

To mitigate the spurious reflections, the four methods of filtering are applied to the coupled simulation. The aforementioned methods in Sect. 3 of bulk viscosity, dissipative time integration and SPML have been re-implemented, as well as the proposed algorithm in Sect. 4. Each of the filtering zones $\Omega_{\mathcal{F}}$ are set to an equal length of $N_{\mathcal{F}} = 50$ elements for comparison. Figure 28a corresponds to the filtering of Fig. 27a, where $\omega_{hf} = \text{L}/68$. At $t = 0.01216$ ms, the incident wave is fully applied to Ω_s and approaches interacting with each of the filtering zones $\Omega_{\mathcal{F}}$ in each of the filtered simulations.

In Fig. 28b, the wave reaches interface Γ between small and large mesh sizes, as well as interacting with $\Omega_{\mathcal{F}}$. Dissipation starts to be evident, especially with the SPML-based and proposed attenuation. In Fig. 28c, the wave propagates through Ω_L, with the spurious reflection evident. Evaluation of the attenuation methods is clear at this time step $t_3 = 0.03647$ ms. The amplitude of the reflections show the SPML and the Shepard-based projection method perform best. The implementation of the proposed method for this

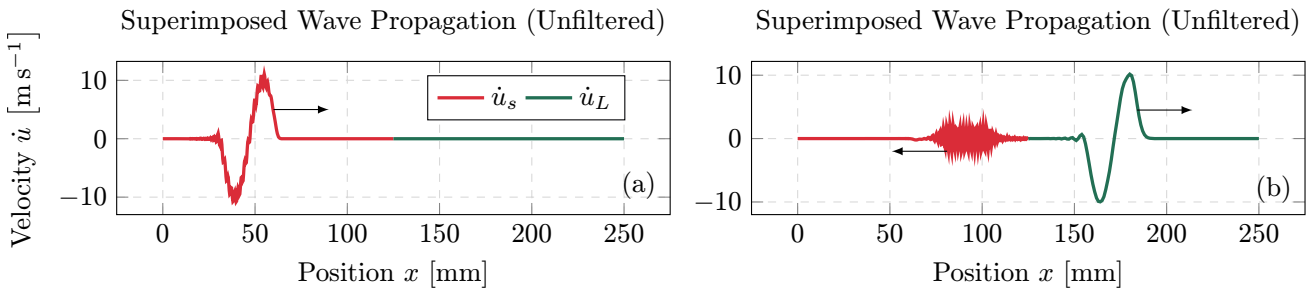

Fig. 27 Velocity distributions of superimposed wave propagation with $\omega_{lf} = L_s/4$ and $\omega_{hf} = \text{L}/68$; **a** incident wave at $t_1 = 0.01216$ ms; **b** transmission and spurious wave reflection at $t_2 = 0.03647$ ms

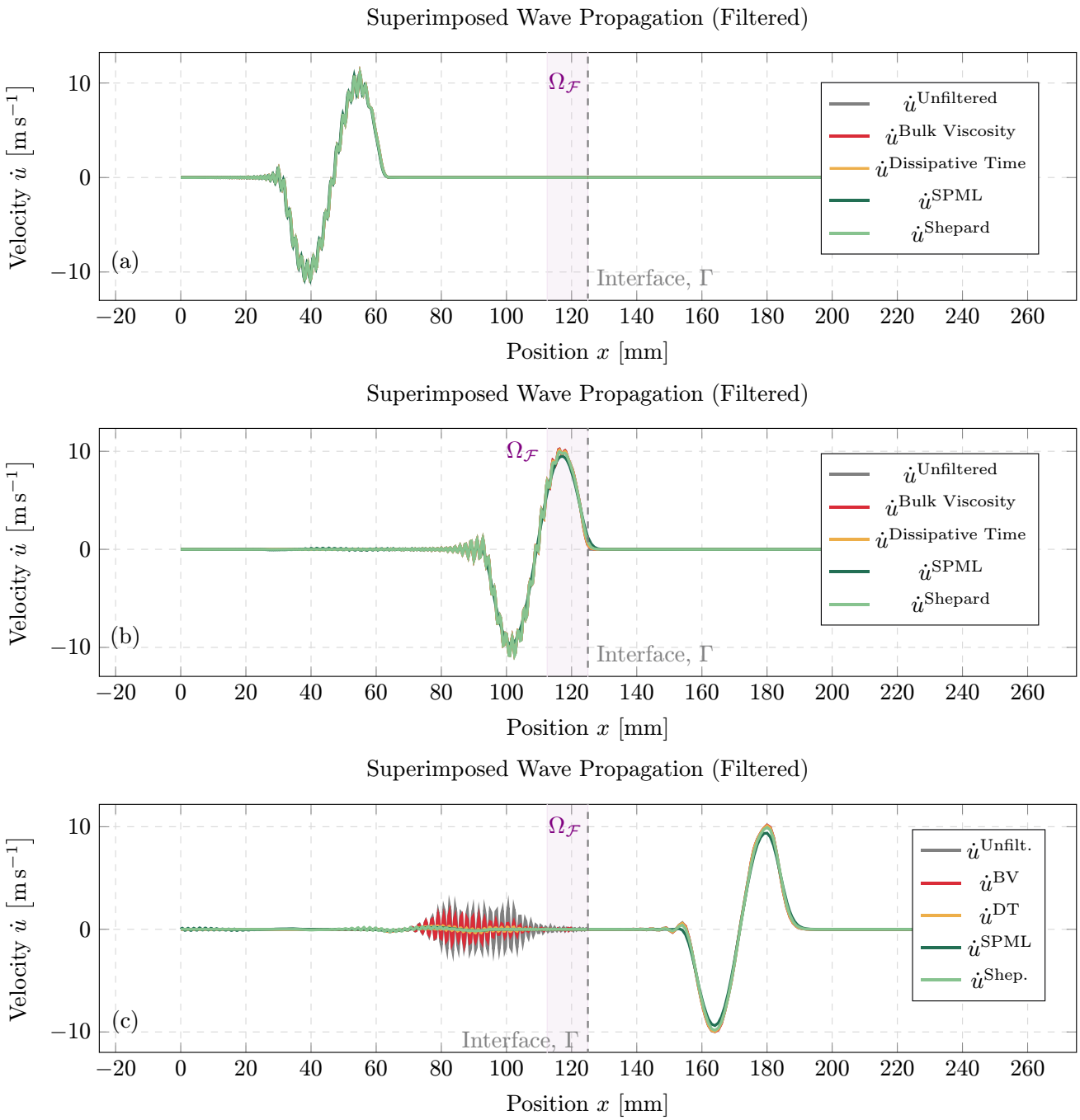

Fig. 28 Comparison of attenuation methods in superimposed wave propagation benchmark with $\omega_{lf} = L_s/4$ and $\omega_{hf} = L_s/68$; **a** incident wave at $t_1 = 0.01216$ ms; **b** transmission and spurious wave reflection at $t_2 = 0.02431$ ms; **c** transmission and spurious wave reflection at $t_3 = 0.03647$ ms

benchmark, can be found in the repository at https://github.com/kinfungchan/spurious-wave.

Acknowledgements This research was supported by the EPSRC and First Light Fusion under the AMPLIFI Prosperity Partnership - EP/X025373/1. The authors also thank the reviewers for their helpful comments, in improving this manuscript.

List of symbols

Roman letters

$\mathbf{A}$	Localised Lagrange multiplier coupling matrix
A	Area
$\mathbf{B}$	Spatial derivatives of shape functions
$\mathbf{b}$	Body forces
$\mathbf{C}$	Incidence matrix (global to interface)
c	Dilatational wave speed
$\boldsymbol{D}$	Rate of deformation
$\mathbf{d}$	Distance matrix
d	Dimension
E	Young's modulus
$\mathbf{f}^{\text{ext}}$	External force
$\mathbf{f}^{\text{int}}$	Internal force
$\mathbf{f}^{\text{kin}}$	Kinetic force
H	Hardening Modulus
h	Characteristic length
$\mathbf{I}$	Identity matrix
i	Index
j	Small node index
k	Large (anchor) node index
$\mathbf{L}$	Incidence matrix (interface to global)
L	Length
$\mathbf{M}$	Mass matrix
m	Ratio of time steps
$\mathcal{N}_{(\cdot)}$	Number of quantity
$\mathbf{N}$	Interpolation (shape) functions
N	Large step
n	Small step
$\mathbb{P}$	Small field projector
P	Power
p	Inverse distance weight order
$\mathbb{Q}$	Large field projector
$\mathbf{R}$	Restriction coupling operator
$\mathbb{R}$	Set of real numbers
r	Radius
$\boldsymbol{t}$	Traction
t	Time
Δt	Time step
$\mathbf{u}$	Displacement
$\dot{\mathbf{u}}$	Velocity
$\ddot{\mathbf{u}}$	Acceleration
W	Work
$\mathbf{w}$	Shepard's Weights
$\mathbf{x}$	Spatial coordinates

Greek symbols

α	Time step reduction factor
β	Dissipative time step factor
Γ	Interface
$\gamma_{\mathcal{F}}$	Filtering coefficient
δ	Variation
ϵ	Tolerance
ε	Strain
ρ	Density
$\boldsymbol{\lambda}$	Localised Lagrange multiplier
λ	Wavelength
ξ	Damping ratio
$\boldsymbol{\sigma}$	Cauchy stress tensor
Ω	Domain
ω	Frequency
∇	Gradient

Superscripts and subscripts

$(\cdot)_C$	Critical (CFL) quantity
$(\cdot)_d$	Damping quantity
$(\cdot)_e$	Element quantity
$(\cdot)_{\mathcal{F}}$	Filtered subdomain quantity
$(\cdot)_\Gamma$	Interface quantity
$(\cdot)_L$	Large subdomain quantity
$(\cdot)_s$	Small subdomain quantity
$(\cdot)^{\mathrm{T}}$	Transpose of quantity
$\check{(\cdot)}$	Mass normalised quantity
$\tilde{(\cdot)}$	Unconstrained quantity

References

1. Bažant ZP, (1978) Spurious reflection of elastic waves in nonuniform finite element grids. Comput Methods Appl Mech Eng 16(1):91–100
2. Bažant ZP, Celep Z (1982) Spurious reflection of elastic waves in nonuniform meshes of constant and linear strain unite elements. Comput Struct 15(4):451–459
3. Celep Z, Bažant ZP (1983) Spurious reflection of elastic waves due to gradually changing finite element size. Int J Numer Meth Eng 19(5):631–646
4. Grunwald C, Durr N, Sauer M, Riedel W, Hiermaier S (2021) A concurrent two-scale coupling for wave propagation using direct solution schemes with explicit time integration. Int J Numer Meth Eng 122(21):6361–6383
5. Berger MJ, Colella P (1989) Local adaptive mesh refinement for shock hydrodynamics. J Comput Phys 82(1):64–84
6. Wellmann C, Wriggers P (2012) A two-scale model of granular materials. Comput Methods Appl Mech Eng 205:46–58
7. Bendezu M, Romanel C, Roehl D (2017) Finite element analysis of blast-induced fracture propagation in hard rocks. Comput Struct 182:1–13
8. De Borst R (2008) Challenges in computational materials science: multiple scales, multi-physics and evolving discontinuities. Comput Mater Sci 43(1):1–15
9. Tang S, Hou TY, Liu WK (2006) A mathematical framework of the bridging scale method. Int J Numer Meth Eng 65(10):1688–1713

10. Sadeghirad A, Tabarraei A (2013) A damping boundary condition for coupled atomistic-continuum simulations. Comput Mech 52(3):535–551
11. Jiang L, Rogers RJ (1990) Effects of spatial discretization on dispersion and spurious oscillations in elastic wave propagation. Int J Numer Meth Eng 29(6):1205–1218
12. Liu J, Sharan S, Yao L (1994) Wave motion and its dispersive properties in a finite element model with distortional elements. Comput Struct 52(2):205–214
13. Idesman A, Samajder H, Aulisa E, Seshaiyer P (2009) Benchmark problems for wave propagation in elastic materials. Comput Mech 43(6):797–814
14. Gottlieb D, Shu C-W (1997) On the gibbs phenomenon and its resolution. SIAM Rev 39(4):644–668
15. Holmes N, Belytschko T (1976) Postprocessing of finite element transient response calculations by digital filters. Comput Struct 6(3):211–216
16. Tadmor E (2007) Filters, mollifiers and the computation of the Gibbs phenomenon. Acta Numer 16:305–378
17. Grunwald C, Sauer M, Stolz A, Hiermaier S (2025) Enhancing efficiency in multiscale simulation: comparing a Lagrange multiplier based approach and a weak staggered coupling with optional spml interface for wave propagation. Int J Numer Meth Eng 126(9):7633
18. VonNeumann J, Richtmyer RD (1950) A method for the numerical calculation of hydrodynamic shocks. J Appl Phys 21(3):232–237
19. Mattsson AE, Rider WJ (2015) Artificial viscosity: back to the basics. Int J Numer Meth Fluids 77(7):400–417
20. Maheo L, Grolleau V, Rio G (2013) Numerical damping of spurious oscillations: a comparison between the bulk viscosity method and the explicit dissipative tchamwa-wielgosz scheme. Comput Mech 51(1):109–128
21. Hulbert GM, Chung J (1996) Explicit time integration algorithms for structural dynamics with optimal numerical dissipation. Comput Methods Appl Mech Eng 137(2):175–188
22. Malakiyeh MM, Shojaee S, Bathe K-J (2019) The bathe time integration method revisited for prescribing desired numerical dissipation. Comput Struct 212:289–298
23. Dvořák R, Kolman R, Fíla T, Falta J, Park K (2023) Explicit asynchronous time scheme with local push-forward stepping for discontinuous elastic wave propagation: one-dimensional heterogeneous cases and Hopkinson bar experiment. Wave Motion 121:103169
24. Soares D Jr (2022) A novel truly explicit time-marching procedure for simple and effective analyses of wave propagation models. Eng Comput 38(Suppl 2):1033–1051
25. Soares D Jr (2022) Three novel truly-explicit time-marching procedures considering adaptive dissipation control. Eng Comput 38(4):3251–3268
26. Marchais J, Chamoin L, Rey C (2017) Wave filtering through a selective perfectly matched layer in multiscale couplings with dynamically incompatible models. Int J Numer Meth Eng 110(8):745–775
27. Berenger J-P (1994) A perfectly matched layer for the absorption of electromagnetic waves. J Comput Phys 114(2):185–200
28. Basu U, Chopra AK (2003) Perfectly matched layers for time-harmonic elastodynamics of unbounded domains: theory and finite-element implementation. Comput Methods Appl Mech Eng 192(11–12):1337–1375
29. Basu U (2009) Explicit finite element perfectly matched layer for transient three-dimensional elastic waves. Int J Numer Meth Eng 77(2):151–176
30. Xiao S, Belytschko T (2004) A bridging domain method for coupling continua with molecular dynamics. Comput Methods Appl Mech Eng 193(17–20):1645–1669
31. Dhia HB, Rateau G (2005) The arlequin method as a flexible engineering design tool. Int J Numer Meth Eng 62(11):1442–1462
32. Tu F, Ling D, Bu L, Yang Q (2014) Generalized bridging domain method for coupling finite elements with discrete elements. Comput Methods Appl Mech Eng 276:509–533
33. Zafati E, Al Hout J (2018) Reflection error analysis for wave propagation problems solved by a heterogeneous asynchronous time integrator. Int J Numer Meth Eng 115(6):651–694
34. Shannon CE (1948) A mathematical theory of communication. Bell Syst Tech J 27(3):379–423
35. Benson DJ (1992) Computational methods in Lagrangian and Eulerian hydrocodes. Comput Methods Appl Mech Eng 99(2–3):235–394
36. Kwon S-B, Prakash A (2025) Coupling composite schemes with different time steps for multi-scale structural dynamics. Int J Multiscale Comput Eng 23(3)
37. Michoski C, Dawson C, Kubatko EJ, Wirasaet D, Brus S, Westerink JJ (2016) A comparison of artificial viscosity, limiters, and filters, for high order discontinuous Galerkin solutions in nonlinear settings. J Sci Comput 66(1):406–434
38. Picklo MJ, Tang Q, Zhang Y, Ryan JK, Tang X-Z (2024) Denoising particle-in-cell data via smoothness-increasing accuracy-conserving filters with application to Bohm speed computation. J Comput Phys 502:112790
39. Marchner P, Bizzarri D, Bériot H (2024) Improved near-field PML absorbing functions for exterior three-dimensional Helmholtz problems. Comput Methods Appl Mech Eng 428:117092
40. Oliveira Barbosa JM, Park J, Kausel E (2012) Perfectly matched layers in the thin layer method. Comput Methods Appl Mech Eng 217:262–274
41. Chern A (2019) A reflectionless discrete perfectly matched layer. J Comput Phys 381:91–109
42. Shepard D (1968) A two-dimensional interpolation function for irregularly-spaced data. Proceedings of the 1968 23rd ACM National Conference. pp 517–524
43. Cover T, Hart P (1967) Nearest neighbor pattern classification. IEEE Trans Inf Theory 13(1):21–27
44. Chan KF, Bombace N, Sahu I, Falco S, Petrinic N (2025) Temporal and spatial coupling methods for the efficient modelling of dynamic solids. Materials 18(5):1080
45. Chan KF, Bombace N, Sap D, Wason D, Falco S, Petrinic N (2025) A multi-time stepping algorithm for the modelling of heterogeneous structures with explicit time integration. Int J Numer Meth Eng 126(1):7638
46. Courant R, Friedrichs K, Lewy H (1967) On the partial difference equations of mathematical physics. IBM J Res Dev 11(2):215–234
47. Park K, Felippa C, Gumaste U (2000) A localized version of the method of Lagrange multipliers and its applications. Comput Mech 24(6):476–490
48. Park K, Felippa C, Rebel G (2002) A simple algorithm for localized construction of non-matching structural interfaces. Int J Numer Meth Eng 53(9):2117–2142
49. Jeong G-E, Song Y-U, Youn S-K, Park K (2020) A new approach for nonmatching interface construction by the method of localized Lagrange multipliers. Comput Methods Appl Mech Eng 361:112728
50. Dvořák R, Kolman R, Mračko M, Kopačka J, Fíla T, Jiroušek O, Falta J, Neuhäuserová M, Rada V, Adámek V et al (2023) Energy-conserving interface dynamics with asynchronous direct time integration employing arbitrary time steps. Comput Methods Appl Mech Eng 413:116110
51. Dvořák R, González JA (2024) On the automatic construction of interface coupling operators for non-matching meshes by optimization methods. Comput Methods Appl Mech Eng 432:117336
52. Rubio R, Ferrer A, Hernández J (2025) Preconditioning iterative solvers via the empirical interscale finite element method (EIFEM). Comput Methods Appl Mech Eng 446:118257

53. Cho SS, Kolman R, González J, Park K (2019) Explicit multistep time integration for discontinuous elastic stress wave propagation in heterogeneous solids. Int J Numer Meth Eng 118(5):276–302
54. González JA, Kolman R, Cho S, Felippa C, Park K (2018) Inverse mass matrix via the method of localized Lagrange multipliers. Int J Numer Meth Eng 113(2):277–295
55. Cimrman R, Kolman R, González JA, Park K (2024) Higher-order inverse mass matrices for the explicit transient analysis of heterogeneous solids. Int J Numer Meth Eng 125(11):7457
56. Belytschko T, Mullen R (1978) Stability of explicit-implicit mesh partitions in time integration. Int J Numer Meth Eng 12(10):1575–1586
57. Gravouil A, Combescure A (2001) Multi-time-step explicit-implicit method for non-linear structural dynamics. Int J Numer Meth Eng 50(1):199–225
58. Chiappa A, Iakovlev S, Marzani A, Giorgetti F, Groth C, Porziani S, Biancolini M (2021) An analytical benchmark for a 2d problem of elastic wave propagation in a solid. Eng Struct 229:111655
59. Pantalé O (2002) An object-oriented programming of an explicit dynamics code: application to impact simulation. Adv Eng Softw 33(5):297–306
60. Ramalho L, Belinha J, Campilho R (2019) The numerical simulation of crack propagation using radial point interpolation meshless methods. Eng Anal Boundary Elem 109:187–198
61. Rubasinghe K, Yao G, Niu J, Tsogtgerel G (2023) Polyharmonic splines interpolation on scattered data in 2d and 3d with applications. Eng Anal Boundary Elem 156:240–250
62. Li X, Ryan JK, Kirby RM, Vuik K (2019) Smoothness-increasing accuracy-conserving (SIAC) filtering for discontinuous Galerkin solutions over nonuniform meshes: superconvergence and optimal accuracy. J Sci Comput 81(3):1150–1180
63. Cavoretto R (2021) Adaptive radial basis function partition of unity interpolation: a bivariate algorithm for unstructured data. J Sci Comput 87(2):41
64. Sun J, Wang W (2026) A localized mesh-free radial basis function-finite difference framework with shape parameter adaptive damping for stable time-domain wave simulation in extreme-contrast media. Comput Mech 1–26